

Using physics-informed neural networks to predict non-Newtonian flows

Chung Jun Yu Chester^a

^aCollege of Design and Engineering, National University of Singapore, Singapore

This manuscript was compiled on July 25, 2023

Non-Newtonian fluids exhibit complex behaviour and pose significant challenges in accurately predicting their flow characteristics. In this paper, we present a novel approach that leverages the power of physics-informed neural networks (PINNs) to predict non-Newtonian fluid flow. PINNs integrate the principles of fluid mechanics with the flexibility of neural networks, offering a promising framework for accurate modelling and simulation of complex fluid systems. By incorporating the constitutive equations that relate shear stress to deformation, we formulate a physics-informed loss function that ensures the network's predictions satisfy the governing equations of the fluid flow. This allows us to capture the time- and rate-dependent material functions that are inherent in non-Newtonian fluids. Additionally, PINNs eliminate the need for explicit mesh generation, reducing computational costs and increasing efficiency. To validate the effectiveness of our approach, we conduct extensive experiments on various non-Newtonian fluids, which are characterized under the Cross Power-Law and Carreau-Yasuda models. We compare our predictions with ground truth data and demonstrate that the physics-informed neural networks achieve high accuracy in capturing the intricate flow behaviour of these fluids under different flow protocols and boundary conditions. Furthermore, we investigate the capability of PINNs to handle cases with unknown boundary conditions by utilizing sparse velocity measurements. Our results showcase the network's ability to accurately reconstruct velocity and stress fields across the entire fluid domain, including the boundaries, providing valuable insights into flow behaviour even in scenarios with limited information. The proposed methodology not only enhances our understanding of non-Newtonian fluid flow but also has significant implications in various industrial and natural settings. The physics-informed neural network approach offers a versatile and efficient tool for predicting and analysing complex fluid systems, providing a bridge between traditional fluid mechanics and modern data-driven techniques. With further advancements and refinements, this approach holds great potential for enhancing design processes, optimization strategies, and decision-making in fluid dynamics applications.

Physics-informed neural network | Non-Newtonian fluid | Flow prediction | Machine learning | Data-driven methods

1. Introduction

1.1. Background on non-Newtonian fluids.

Non-Newtonian fluids are a diverse class of materials that do not adhere to Newton's law of viscosity, which states that the shear stress within a fluid is directly proportional to the rate of shear strain (1). Unlike Newtonian fluids, non-Newtonian fluids exhibit complex and often time-dependent flow behaviours (2). They can be found in various natural and industrial settings, making their accurate prediction and modelling essential. Non-Newtonian fluids encompass a wide range of materials, including polymer solutions, suspensions, gels, emulsions, and biological fluids. Understanding their flow behaviour is crucial in numerous fields such as chemical processing, oil and gas transportation, food manufacturing, and biomedical engineering.

One prominent characteristic of non-Newtonian fluids is shear-thinning behaviour, also known as pseudoplasticity (3). Certain fluids, such as those containing long-chain polymers or suspended particles, exhibit a decrease in viscosity as the shear rate increases. As the fluid experiences higher shear rates, the internal structure is disrupted, reducing the resistance to flow (4). Shear-thinning behaviour is widely observed in everyday substances like ketchup, paint, and shampoo, which flow more easily under shear stress. In contrast, some non-Newtonian fluids exhibit shear-thickening behaviour, also known as dilatancy. These fluids experience an increase in viscosity as the shear rate rises (5). Dense particle suspensions or fluids with complex microstructures often display this behaviour. For example, a mixture of cornstarch and water, known as oobleck, shows shear-thickening properties when subjected to rapid shear stress (6).

Another significant type of non-Newtonian behaviour is yield stress, which is a minimum shear stress required to initiate flow (7). Until the applied stress exceeds the yield stress, these fluids behave as solids, resisting deformation. Once the yield stress is surpassed, the fluid transitions into a flowing state. Such behaviour is observed in materials like toothpaste, clay suspensions, and certain drilling fluids used in the oil and gas industry. A Bingham plastic is a type of non-Newtonian fluid that exhibits a yield stress behaviour (8). Unlike Newtonian fluids which flow continuously under any shear stress, a Bingham plastic requires a certain minimum shear stress, known as the yield stress, to initiate flow. Below the yield stress, a Bingham plastic behaves like a solid and does not flow. However, once the applied shear stress exceeds the yield stress, the Bingham plastic transitions into a flowing state and exhibits a linear relationship between shear stress and shear rate, similar to a Newtonian fluid (9). In the field of rheology, Bingham plastics are extensively studied and characterized to understand their flow behaviour. Experimental techniques, such as rotational viscometry, are commonly employed to determine the yield stress and plastic viscosity of Bingham plastics. Understanding the behaviour of Bingham plastics is crucial for various applications, including drilling fluids, coatings, paints, and food processing (10), where their flow properties play a significant role in process optimization and performance. The differences in the relationships between shear stress and viscosity against shear rate for Bingham plastic, pseudoplastic, dilatant and Newtonian fluid are illustrated in Figures 1a and 1b respectively.

Viscoelastic fluids exhibit both viscous (fluid-like) and elastic (solid-like) characteristics, displaying time-dependent responses

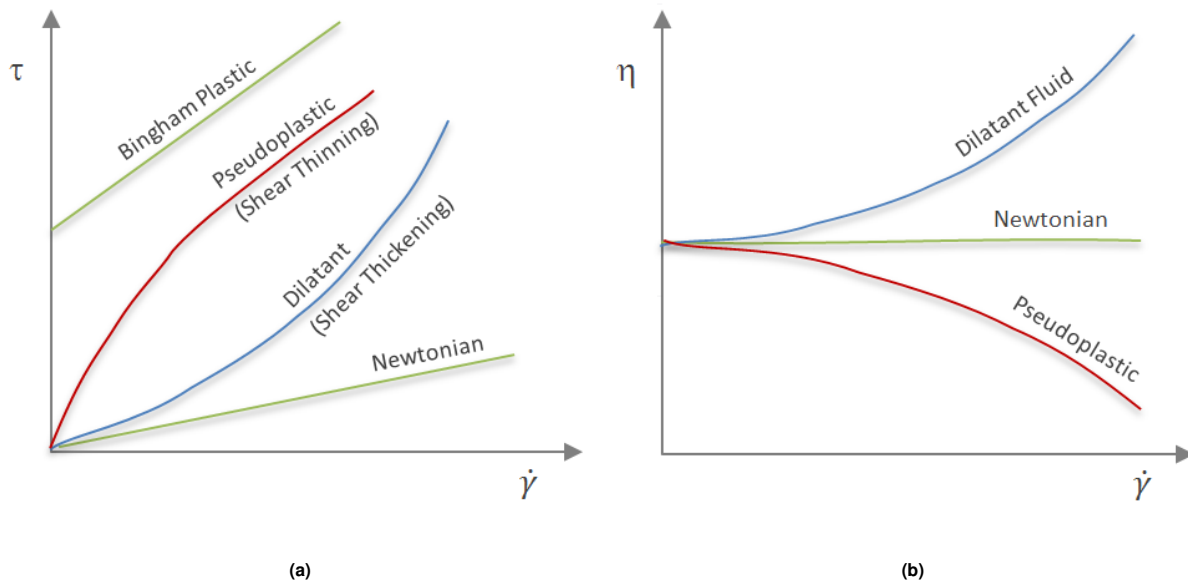


Fig. 1. (a) Variation of shear stress over shear strain for Bingham Plastic, pseudoplastic, dilatant fluid, and Newtonian fluid (11). **(b)** Variation of viscosity over shear strain for dilatant fluid, Newtonian fluid, and pseudoplastic (11).

to stress or deformation (12). They can store and release energy over time, exhibiting behaviours like stress relaxation and creep. Examples of viscoelastic fluids include polymer melts, biological fluids like blood, and materials used in soft robotics. Understanding and characterizing the behaviour of non-Newtonian fluids pose significant challenges. Their complex flow behaviour arises from factors such as composition, concentration, temperature, and applied shear rate or stress (13). The presence of suspended particles, polymers, surfactants, or other additives can dramatically influence their rheological properties.

Modelling non-Newtonian fluid flow requires appropriate constitutive models that describe the relationship between stress, strain, and deformation history. The complexity of non-Newtonian behaviour necessitates the use of constitutive equations that capture phenomena like thixotropy, strain history dependence, and multiple regimes of flow behaviour (14). Experimentation and characterization of non-Newtonian fluids can be challenging due to the need for specialized equipment and techniques. Moreover, computational modelling of non-Newtonian fluid flow involves solving complex partial differential equations and incorporating constitutive models, often requiring advanced computational methods.

Understanding the complex flow behaviour of non-Newtonian fluids is vital in numerous fields. Accurate modelling of non-Newtonian fluid flow plays a crucial role in optimizing industrial processes, designing efficient transport systems, ensuring product quality, and enhancing performance in various applications (15). In biological and medical fields, non-Newtonian fluid behaviour is significant in understanding blood flow (16), mucus transport, drug delivery, and other physiological processes. Furthermore, non-Newtonian fluid flow is relevant in natural phenomena such as sediment transport in rivers, landslides, and lava flow. By comprehending the intricate nature of non-Newtonian fluids and the factors influencing their flow behaviour, researchers can develop accurate models and computational methods to predict and optimize the flow of these complex fluids. This understanding enables advancements in a wide range of fields, contributing to technological innovations and improvements in engineering, medicine, and environmental sciences.

1.2. Motivation of study.

Accurately predicting the flow behaviour of non-Newtonian fluids is of utmost importance due to its significant implications across a wide range of industries and scientific fields. The motivation for achieving accurate predictions stems from several key factors, driving the need for improved understanding and modelling of non-Newtonian fluid flow. One primary motivation lies in industrial applications. Many industrial processes involve the handling and transportation of non-Newtonian fluids, such as in chemical processing (17), oil and gas production, food manufacturing, and cosmetics production. In these industries, the behaviour of non-Newtonian fluids directly affects process efficiency, product quality, and overall operational performance. Accurate prediction of flow behaviour enables better process optimization (15), reduces energy consumption, minimizes waste, and enhances product consistency.

Transportation of non-Newtonian fluids through pipelines is another critical application area. Understanding their flow

The author designed the study, analysed the data, drafted the manuscript, and revised it critically for important intellectual content. The author approved the final version of the manuscript for submission.

behaviour is essential in designing efficient transportation systems for substances like slurries, drilling muds (18), and polymer solutions. Accurate predictions enable engineers to determine pipeline sizing, evaluate pressure drop and pumping requirements (19), and mitigate issues such as clogging or blockages that can occur due to complex flow behaviours. In the field of biomedical engineering, accurate modelling of non-Newtonian fluid flow is crucial for understanding physiological processes and developing medical devices and treatments. Blood flow, for instance, exhibits non-Newtonian behaviour due to its complex composition and rheological properties. Accurate predictions of blood flow behaviour help in diagnosing and treating cardiovascular diseases, designing artificial organs, and improving drug delivery systems (20).

The accurate prediction of non-Newtonian fluid flow is also vital in environmental sciences and geophysical applications. Understanding sediment transport in rivers, landslides, and volcanic lava flow (21) requires accurate modelling of non-Newtonian behaviour. Accurate predictions aid in hazard assessment, environmental impact assessment, and effective management of natural resources. Furthermore, the development of innovative technologies, such as 3D printing and additive manufacturing (22), increasingly relies on accurate predictions of non-Newtonian fluid flow. Controlling the flow behaviour of materials with complex rheological properties is essential for achieving precise deposition and fabrication processes, ensuring the structural integrity and quality of the printed objects (22).

Overall, the motivation for accurate prediction of non-Newtonian fluid flow arises from the desire to enhance process efficiency, product quality, and operational performance in industrial applications. It extends to medical and biomedical fields, enabling improved understanding and treatment of physiological processes. Accurate predictions also support environmental sciences, geophysics, and the development of cutting-edge technologies. Advancements in accurate prediction methods for non-Newtonian fluid flow offer numerous benefits, including cost reduction, increased safety, improved process control, and enhanced product design and development (15). By bridging the gap in understanding and modelling non-Newtonian flow behaviour, researchers can drive innovation and create a positive impact on various industries, improving efficiency, sustainability, and technological advancements.

1.3. Overview of physics-informed neural networks (PINNs).

Physics-Informed Neural Networks (PINNs) have emerged as a promising approach for modelling and predicting complex fluid flow, including the behaviour of non-Newtonian fluids (23). This section provides a detailed overview of PINNs and highlights their potential as a tool for accurately modelling non-Newtonian fluid flow.

Neural networks are mathematical models inspired by the structure and functioning of biological neural networks (24). In the field of fluid mechanics, neural networks have gained attention for their ability to approximate and capture intricate flow behaviours by learning from data. PINNs, specifically, take this concept a step further by incorporating the governing equations of fluid mechanics into the neural network architecture, making them "physics-informed" (23). By integrating the physics equations, PINNs ensure that the predicted flow fields satisfy the fundamental laws of fluid dynamics. This physics-informed approach offers several advantages for modeling non-Newtonian fluid flow. Non-Newtonian fluids exhibit complex behaviours such as shear thinning, shear thickening, and yield stress effects. These behaviours are challenging to capture accurately with traditional modelling approaches (25).

PINNs, with their capacity to approximate highly nonlinear functions, are well-suited to capture and model the intricate behaviour exhibited by non-Newtonian fluids. They can seamlessly incorporate the constitutive models that relate stress, strain, and deformation history in non-Newtonian fluids. By including these constitutive models as additional physics constraints in the loss function, PINNs can accurately represent the non-Newtonian behaviour (26). Another significant advantage of PINNs is their mesh-free and flexible framework. Unlike traditional computational fluid dynamics methods, PINNs do not require explicit mesh generation, reducing computational costs and offering greater flexibility in handling complex geometries (27). Non-Newtonian fluids often exhibit complex flow patterns and non-uniform domains, making the mesh-free nature of PINNs particularly advantageous. PINNs can handle irregularly spaced data and adaptively refine predictions, providing more accurate flow field representations. They leverage advanced optimization techniques and automatic differentiation to efficiently train the network and minimize the loss function (28). Once trained, PINNs can rapidly predict flow fields, enabling real-time simulations and optimization in various engineering and scientific applications.

While PINNs offer great promise for modelling non-Newtonian fluid flow, there are challenges and considerations to address. The availability of high-quality and representative training data is crucial for accurate PINN predictions. Generating or acquiring diverse and comprehensive datasets for non-Newtonian fluids can be challenging, requiring careful experimental design or advanced numerical simulations (29). Additionally, selecting an appropriate network architecture and determining optimal hyperparameters significantly impact the accuracy and convergence of PINN predictions. Fine-tuning the network architecture and hyperparameters for specific non-Newtonian fluid behaviours and constitutive models is an ongoing area of research. Interpretability of PINNs can be challenging, hindering the physical insight gained from the model's predictions (26). Researchers are actively exploring techniques to improve interpretability and gain a deeper understanding of the underlying flow physics captured by PINNs.

Furthermore, quantifying uncertainties in PINN predictions, especially for non-Newtonian fluid flow, is an area of active research. Developing robust methods for uncertainty quantification can provide a measure of confidence and reliability in the predictions, enhancing the applicability and trustworthiness of PINNs in practical engineering scenarios. Nevertheless, PINNs offer a promising tool for accurately modelling non-Newtonian fluid flow. Their ability to capture complex flow behaviour, integrate constitutive models, and provide a flexible mesh-free framework makes them well-suited for predicting the behaviour of non-Newtonian fluids. Addressing challenges related to data availability, network architecture, interpretability, and uncertainty quantification will further unlock the potential of PINNs in modelling non-Newtonian fluid flow. Continued advancements in this

field will enhance our understanding and predictive capabilities, leading to improved design, optimization, and decision-making in various practical applications.

1.4. Research objectives and scope of paper.

The primary objective of this research paper is to explore and demonstrate the potential of using physics-informed neural networks (PINNs) as a tool for accurately predicting non-Newtonian fluid flow. By leveraging the strengths of neural networks and incorporating the physics equations governing fluid dynamics, PINNs offer a promising approach to model and understand the complex behaviour exhibited by non-Newtonian fluids. This section outlines the specific research objectives and the scope of the paper. The research aims to address the following key objectives:

1. Investigate the applicability of PINNs for non-Newtonian fluid flow: The paper will assess the suitability of PINNs in capturing the complex behaviours exhibited by non-Newtonian fluids, including shear thinning, shear thickening, and yield stress effects. By incorporating the relevant constitutive models and physics constraints, the effectiveness of PINNs in representing the intricate flow behaviour of non-Newtonian fluids will be evaluated.

2. Develop a framework for integrating non-Newtonian behaviour into PINNs: The paper will present a methodology for incorporating constitutive models and physics constraints into the PINN framework to accurately capture the non-Newtonian fluid flow behaviour. Techniques for handling time-dependent behaviours and memory effects will be explored and integrated into the PINN architecture.

3. Validate and assess the accuracy of PINN predictions: Extensive validation experiments will be conducted to compare the predictions of the PINN model with experimental or benchmark data for a variety of non-Newtonian fluid flow scenarios. The accuracy and reliability of PINN predictions in capturing the complex flow behaviour of non-Newtonian fluids will be quantitatively evaluated, and the strengths and limitations of the approach will be identified.

The scope of the paper encompasses a range of non-Newtonian fluid flow scenarios, and different constitutive models and behaviours will be considered to capture the diverse characteristics exhibited by non-Newtonian fluids. The focus will be on developing a comprehensive understanding of the applicability, accuracy, and limitations of PINNs in modelling non-Newtonian fluid flow. The research will primarily utilize numerical simulations to validate the effectiveness of the PINN approach. The paper will also discuss the implications and potential applications of using PINNs for non-Newtonian fluid flow modelling in various fields, including industrial processes, biomedical engineering, and environmental sciences. Practical considerations, such as computational efficiency, model interpretability, and uncertainty quantification, will be discussed, highlighting areas for further research and development.

Overall, this research paper aims to contribute to the understanding and advancement of non-Newtonian fluid flow modelling by demonstrating the potential and efficacy of physics-informed neural networks. By addressing the research objectives outlined above and discussing the scope and implications of the findings, the paper will provide valuable insights into the use of PINNs as a tool for accurately predicting and understanding non-Newtonian fluid flow behaviour.

2. Non-Newtonian fluid behaviour and Constitutive models

2.1. Shear Thinning and Shear Thickening behaviour.

Non-Newtonian fluids exhibit complex behaviour that deviates from the linear relationship between shear stress and shear rate described by Newton's law of viscosity (1). Understanding non-Newtonian fluid behaviour is essential for a wide range of applications in various industries and scientific fields. This section provides a brief explanation of non-Newtonian fluid behavior and discusses the challenges associated with modelling and characterizing these fluids.

Shear-thinning behavior (pseudoplasticity) is a common characteristic of non-Newtonian fluids, wherein the viscosity of the fluid decreases as the shear rate increases (3). To understand shear-thinning behavior in non-Newtonian fluids, it is necessary to explore the underlying mechanisms and factors that contribute to this phenomenon. In Newtonian fluids, the viscosity remains constant regardless of the applied shear rate. However, non-Newtonian fluids exhibit a more complex response to shear, with viscosity depending on the shear rate or shear stress. Shear-thinning behavior is particularly prevalent in fluids containing long-chain polymers, such as polymer solutions or polymer melts, as well as colloidal suspensions and certain biological fluids (30). The shear-thinning behavior arises due to the behavior of the fluid's microstructure under deformation. When a non-Newtonian fluid experiences shear, the internal structure or arrangement of its constituent particles or molecules changes. This structural reorganization can result in a reduction in the fluid's resistance to flow, leading to a decrease in apparent viscosity. One mechanism contributing to shear-thinning behavior is the alignment or stretching of polymer chains in polymer solutions or melts (31). At low shear rates, the polymer chains are entangled and hinder the flow, resulting in higher viscosity. As the shear rate increases, the chains align and slide past each other more easily, reducing the resistance to flow and causing a decrease in viscosity. This alignment and stretching of polymer chains is often referred to as "shear-induced alignment" (32). In colloidal suspensions, shear-thinning behavior can occur due to the disruption of particle networks. At low shear rates, the particles form interconnected networks that impede flow, leading to a higher viscosity. As shear is applied, the particle networks start to break down, resulting in a decrease in resistance to flow and a decrease in viscosity (32). The underlying mechanisms responsible for shear-thinning behavior in biological fluids, such as blood or mucus, can be complex and involve interactions between different components. For example, in blood, the presence of red blood cells and their deformability contribute to the shear-thinning behavior (33). At low shear rates, the cells aggregate and hinder flow, causing an increase in viscosity. As the shear rate increases, the cells align and deform, reducing the resistance to flow and resulting in shear thinning. Mathematically, shear-thinning behavior can be described by various constitutive models, such as the Power-Law

model or the Carreau-Yasuda model. These models incorporate empirical parameters that capture the relationship between shear stress, shear rate, and viscosity. Shear-thinning behavior is a key characteristic of non-Newtonian fluids, resulting in a decrease in viscosity as the shear rate increases. This behavior arises from the reorganization of the fluid's microstructure or the deformation and alignment of constituent particles or polymers. Understanding the underlying mechanisms and employing appropriate constitutive models allow for accurate prediction and manipulation of shear-thinning behavior in non-Newtonian fluids.

Shear thickening behavior is a phenomenon observed in certain non-Newtonian fluids where the viscosity of the fluid increases as the shear rate or shear stress increases. This behavior, also known as dilatancy or shear-induced thickening (5), is the opposite of shear-thinning behavior. Understanding shear thickening in non-Newtonian fluids requires exploring the underlying mechanisms and factors that contribute to this phenomenon. In Newtonian fluids, the viscosity remains constant, independent of the applied shear rate. However, in non-Newtonian fluids, such as suspensions of solid particles in a liquid, shear thickening can occur due to the interactions and rearrangement of particles under shear (34). As the shear rate or shear stress increases, the particles interact more strongly and form temporary networks or structures within the fluid. These networks hinder the flow, leading to an increase in the apparent viscosity. The mechanism behind shear thickening behavior can be explained by the concept of hydrodynamic lubrication and particle interactions (35). At low shear rates, the fluid lubricates the particles, allowing them to flow past each other with minimal resistance. However, as the shear rate increases, the fluid between the particles gets squeezed out, causing the particles to come into closer contact and leading to increased friction and resistance to flow. This particle-particle interaction contributes to the observed shear thickening behavior.

The exact nature of shear thickening can vary depending on the specific characteristics of the fluid system. In some cases, the thickening behavior is abrupt and occurs at a specific critical shear rate, often referred to as the "shear thickening transition" (36). Beyond this critical shear rate, the viscosity can increase significantly. In other cases, shear thickening can occur gradually over a range of shear rates, resulting in a more continuous increase in viscosity. Mathematically, shear thickening behavior can be described using various constitutive models, such as the Cross model or the Krieger-Dougherty model (37). These models incorporate empirical parameters to capture the relationship between shear stress, shear rate, and viscosity. The Cross model, for example, describes shear thickening with an exponential function, while the Krieger-Dougherty model accounts for particle volume fraction and provides a more general description of the viscosity as a function of shear rate (37). The understanding and control of shear thickening behavior in non-Newtonian fluids have practical implications in various industries and applications. For instance, shear thickening fluids are used in protective gear and armor to enhance impact resistance (38). Understanding the underlying mechanisms and optimizing the formulation of these fluids can lead to improved performance and enhanced protection. In summary, shear thickening behavior is a characteristic of certain non-Newtonian fluids where the viscosity increases as the shear rate or shear stress increases. This behavior arises due to particle-particle interactions and the formation of temporary networks within the fluid. Understanding the mechanisms and employing appropriate constitutive models allow for accurate prediction and control of shear thickening behavior in non-Newtonian fluids.

Modelling and characterizing non-Newtonian fluid behaviour present significant challenges due to their complexity. These challenges include:

1. Nonlinear Rheology: Non-Newtonian fluids often exhibit highly nonlinear relationships between shear stress, shear rate, and viscosity (39). This nonlinearity poses challenges in developing accurate constitutive models that describe the flow behaviour of these fluids.

2. Complex Constitutive Models: The behaviour of non-Newtonian fluids is typically described by constitutive models that relate stress, strain, and deformation history. Selecting appropriate models and parameters that capture the wide range of behaviours exhibited by different non-Newtonian fluids is challenging.

3. Experimental Characterization: Experimental techniques for characterizing non-Newtonian fluid behaviour can be complex and require specialized equipment. Measuring and quantifying properties such as viscosity, yield stress, and time-dependent responses can be challenging due to the variability and sensitivity of these fluids.

4. Computational Modelling: Numerical simulation of non-Newtonian fluid flow involves solving complex partial differential equations and incorporating constitutive models. The computational cost and complexity increase with the inclusion of complex flow behaviours and non-uniform domains.

5. Parameter Sensitivity: Non-Newtonian fluid behaviour can be sensitive to various factors such as concentration, temperature, and shear rate. Small variations in these parameters can lead to significant variations in the fluid's rheological properties, making accurate prediction and modelling challenging.

Addressing these challenges is essential to improve our understanding and modelling capabilities of non-Newtonian fluid behaviour. Overcoming these obstacles will lead to more accurate predictions, better process design, and optimization in industries such as chemical processing, oil and gas, food manufacturing, and biomedical engineering. Advances in experimental techniques, computational methods, and constitutive modelling will contribute to enhancing our knowledge of non-Newtonian fluid behaviour and its practical applications.

2.2. Non-Newtonian constitutive models.

In the field of non-Newtonian fluid mechanics, a variety of constitutive models have been developed to describe and characterize the complex flow behaviour exhibited by these fluids. These models provide mathematical relationships between stress, strain, and deformation history, enabling accurate predictions and simulations. This section provides an overview of some commonly used non-Newtonian constitutive models and their key characteristics.

1. Power-Law Model: The Power-Law model, also known as the Ostwald-de Waele model, is one of the simplest and most widely used constitutive models for non-Newtonian fluids. It describes the relationship between shear stress (τ) and shear rate ($\dot{\gamma}$) using a power-law equation:

$$\tau = K\dot{\gamma}^n \quad [1]$$

Here, K is the flow consistency index and n is the power law exponent. The Power-Law model is commonly employed for fluids exhibiting shear-thinning or shear-thickening behaviour. If n is smaller than a value of 1, the fluid is characterized as a pseudoplastic. Whereas, if n is larger than a value of 1, the fluid is characterized as a dilatant. If n is exactly equals to 1, the fluid is a Newtonian fluid. One example of a fluid governed by the Power-Law model is a mixture of cornstarch and water, also known as oobleck.

2. Herschel-Bulkley Model: The Herschel-Bulkley model extends the Power-Law model by incorporating a yield stress (τ_y) component (40). It is suitable for fluids that require a minimum shear stress to initiate flow. The Herschel-Bulkley model is given by the equation:

$$\tau = \tau_y + K\dot{\gamma}^n \quad [2]$$

The parameters τ_y , K , and n represent the yield stress, flow consistency index, and flow behaviour index, respectively. This model effectively captures the yield stress behaviour observed in materials such as drilling fluids, pastes, and gels.

3. Bingham Model: The Bingham model is a simplified form of the Herschel-Bulkley model that describes materials with a yield stress but no shear thinning or shear thickening (8). It is characterized by a linear relationship between shear stress and shear rate beyond the yield point. The Bingham model is expressed as:

$$\tau = \tau_y + \eta\dot{\gamma} \quad [3]$$

Here, η is the plastic viscosity and represents the fluid's resistance to flow beyond the yield stress.

4. Carreau-Yasuda Model: The Carreau-Yasuda model is commonly used to describe the behaviour of viscoelastic fluids, particularly those exhibiting shear-thinning behaviour. It incorporates a relaxation time component to capture time-dependent responses. The Carreau-Yasuda model is given by the equation:

$$\tau = \tau_\infty + (\tau_0 - \tau_\infty)[1 + (\dot{\gamma}\lambda)^a]^{\frac{n-1}{a}} \quad [4]$$

In this model, τ_∞ is the asymptotic shear stress at high shear rates, τ_0 is the shear stress at zero shear rate, λ is the relaxation time constant, a is the power-law index at low shear rates, and n is the power-law index at high shear rates.

5. Cross Power-Law Model: The Cross Power-Law model is a comprehensive viscoelastic constitutive model that accounts for both elastic and viscous components. The model provides an accurate representation of viscoelastic effects, including stress relaxation and elastic recoil. The Cross Power-Law model is expressed as:

$$\nu = \nu_\infty + \frac{\nu_0 - \nu_\infty}{1 + (K\dot{\gamma})^n} \quad [5]$$

In this model, ν_0 and ν_∞ refer to the zero-shear-rate viscosity and infinite-shear-rate viscosity respectively. $\dot{\gamma}$ refers to the shear rate, while K and n refer to the flow consistency index and the power law exponent respectively.

These constitutive models represent a subset of the many available models used to describe the complex flow behaviour of non-Newtonian fluids. Each model captures specific aspects of non-Newtonian behaviour and is suitable for different types of fluids and flow conditions. Selecting the appropriate model depends on the nature of the fluid, the desired accuracy, and the specific flow regime of interest.

It is important to note that while these constitutive models provide a mathematical representation of non-Newtonian behaviour, they are based on simplifications and assumptions. The challenge lies in accurately determining the model parameters through experimental characterization or fitting to data. Additionally, some non-Newtonian fluids may exhibit behaviours that cannot be fully captured by these simplified models, necessitating the development of more sophisticated and specialized constitutive models. Therefore, understanding and utilizing non-Newtonian constitutive models are crucial for accurately modelling and predicting the flow behaviour of these complex fluids. The selection of an appropriate model depends on the specific characteristics and behaviours of the fluid under consideration. By employing these models, researchers and engineers can gain insights into the flow dynamics of non-Newtonian fluids, enabling improved design, optimization, and decision-making in various practical applications.

2.3. Limitations of traditional approaches in modelling non-Newtonian fluid flow.

Modelling the behaviour of non-Newtonian fluids presents unique challenges due to their complex and diverse flow characteristics. Traditional approaches in fluid mechanics have limitations when it comes to accurately capturing the intricate behaviour exhibited by these fluids. This section discusses the limitations and complexities of traditional approaches in modelling non-Newtonian fluid flow.

1. Linear Viscosity Assumption: One of the fundamental limitations of traditional approaches is the linear viscosity assumption inherent in Newtonian fluid models. Traditional models assume a constant viscosity, which does not adequately

capture the varying viscosity observed in non-Newtonian fluids. The non-linear relationship between shear stress and shear rate necessitates the use of constitutive models that go beyond the linear viscosity assumption.

2. Inadequate Representation of Shear-Dependent Behaviour: Non-Newtonian fluids often exhibit shear-dependent behaviour, such as shear thinning or shear thickening. Traditional approaches fail to accurately represent these behaviours due to their simplistic assumptions. Linear models cannot capture the complex relationships between shear stress, shear rate, and other influencing factors, leading to inaccurate predictions.

3. Ignoring Time-Dependent Effects: Many non-Newtonian fluids exhibit time-dependent behaviour, including viscoelasticity and thixotropy. Traditional approaches often neglect these effects or oversimplify them, leading to incomplete representations of fluid behaviour. Ignoring time-dependent effects can result in inaccurate predictions of flow dynamics, especially in scenarios where flow history and deformation play a significant role.

4. Computational Challenges: Numerical simulations of non-Newtonian fluid flow using traditional approaches can be computationally demanding and complex. These methods typically involve solving partial differential equations (PDEs) coupled with constitutive models, often requiring sophisticated numerical techniques and high computational resources. The presence of complex flow behaviour, non-uniform domains, and boundary conditions further complicates the computational modelling process (41).

5. Experimental Characterization: Accurate modelling of non-Newtonian fluid flow requires reliable and comprehensive experimental data for model validation and parameter estimation. However, experimental characterization of non-Newtonian fluids can be challenging and time-consuming. Obtaining accurate measurements of properties such as viscosity, yield stress, and time-dependent responses often requires specialized equipment and techniques.

6. Limited Flexibility in Handling Complex Geometries: Traditional approaches, such as finite element or finite difference methods, often rely on structured meshes, which can limit their ability to handle complex geometries encountered in non-Newtonian fluid flow (42). The generation and adaptation of meshes become more challenging as the complexity of the flow behaviour and domain increases.

Addressing these limitations and complexities requires the development of advanced modelling approaches that can effectively capture the non-linear, time-dependent, and complex behaviours exhibited by non-Newtonian fluids. The emerging field of physics-informed neural networks (PINNs) holds promise in overcoming some of these challenges by integrating the governing equations of fluid mechanics into neural network architectures. PINNs offer a data-driven approach that can capture the intricate flow behaviour and incorporate constitutive models while avoiding the need for explicit mesh generation. Furthermore, advancements in experimental techniques for characterizing non-Newtonian fluids, along with the availability of high-performance computing resources, contribute to improving our understanding and modelling capabilities. The integration of experimental data, computational modelling, and advanced constitutive models will pave the way for more accurate predictions and simulations of non-Newtonian fluid flow.

Overall, traditional approaches in modelling non-Newtonian fluid flow have inherent limitations when it comes to capturing the complex behaviour exhibited by these fluids. The linear viscosity assumption, inadequate representation of shear-dependent and time-dependent behaviour, computational challenges, and experimental limitations hinder accurate predictions. Overcoming these limitations requires the development of advanced modelling techniques and the integration of experimental and computational methods. By addressing these challenges, researchers and engineers can enhance our understanding and predictive capabilities of non-Newtonian fluid flow, enabling improved design, optimization, and decision-making in various practical applications.

3. Physics-Informed Neural Networks (PINNs)

3.1. Description of the architecture and components of PINNs.

Physics-Informed Neural Networks (PINNs) are a specialized type of neural network architecture that incorporates the governing equations of fluid mechanics into their framework. This section provides a detailed description of the architecture and components of PINNs, highlighting their unique design for modelling complex fluid flow behaviour. The architecture of a general PINN is illustrated below in Figure 2.

1. Neural Network Architecture: At the core of PINNs lies a neural network, which consists of interconnected nodes, or neurons, organized into layers. The architecture of the neural network can vary depending on the specific problem and complexity of the flow behaviour being modelled. Common architectures include feedforward neural networks (43), convolutional neural networks (CNNs) (44), or recurrent neural networks (RNNs) (45).

2. Input Layer: The input layer of the neural network receives the input variables that describe the flow conditions, geometry, boundary conditions, or any other relevant parameters. These inputs act as the basis for predicting the flow fields or other desired outputs.

3. Hidden Layers: Between the input and output layers, one or more hidden layers can exist. These hidden layers perform computations and transformations on the inputs, extracting complex patterns and relationships within the data (46). The number of hidden layers and the number of neurons in each layer are design choices that depend on the complexity of the problem and the size of the available dataset.

4. Activation Functions: Activation functions introduce nonlinearity into the neural network, enabling it to capture complex relationships between inputs and outputs. Common activation functions include sigmoid, tanh, or rectified linear unit (ReLU) functions (47). The choice of activation function depends on the specific characteristics of the problem and the desired behaviour of the neural network.

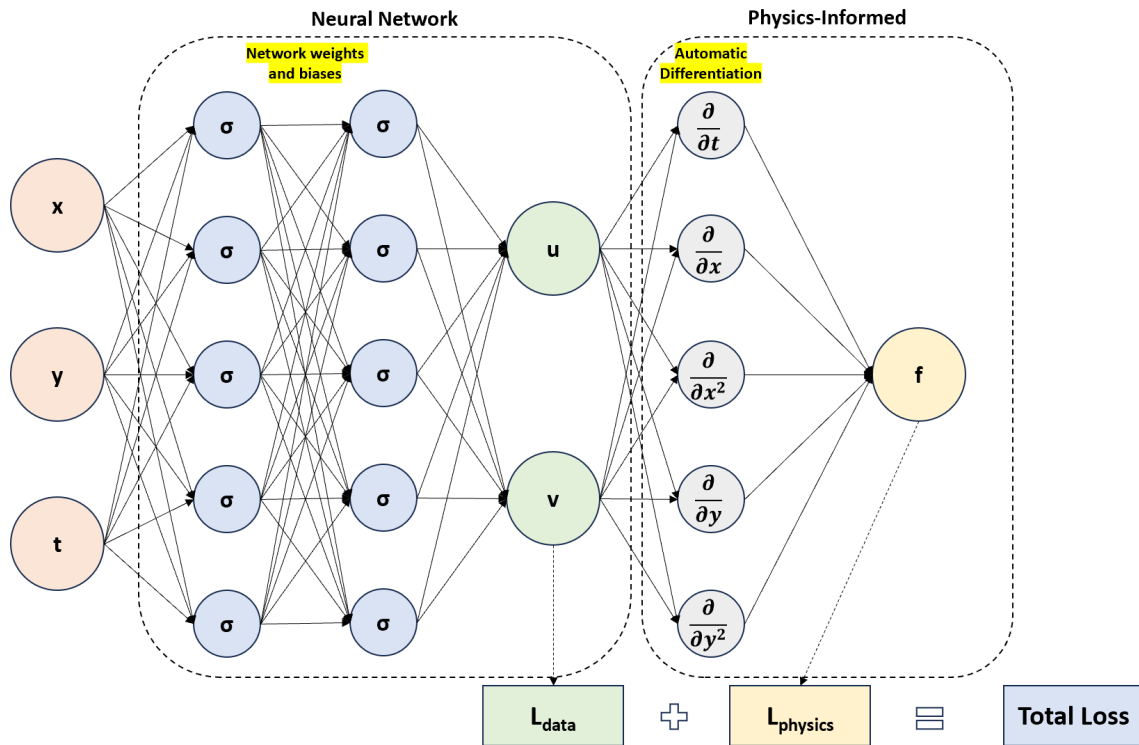


Fig. 2. Architecture of a general Physics-informed neural network. The total loss is computed through the sum of the loss from the data (L_{data}), including losses from the initial and boundary conditions, and the loss from the governing equations ($L_{physics}$).

5. Output Layer: The output layer of the neural network provides the predicted flow fields or other desired outputs, such as pressure, velocity profiles, or stress distributions. The number of neurons in the output layer corresponds to the number of output variables or desired predictions.

6. Physics-informed Loss Function: A key component of PINNs is the physics-informed loss function, which incorporates the governing equations of fluid mechanics as constraints in the optimization process. By including these constraints, PINNs ensure that the predicted flow fields satisfy the fundamental laws of fluid dynamics. The loss function consists of two terms: a data-fitting term that compares the predicted outputs with the available data and a physics-based term that enforces the governing equations (48).

7. Automatic Differentiation: Automatic Differentiation plays a vital role in PINNs by allowing efficient calculation of derivatives with respect to the network parameters (49). PINNs utilize automatic differentiation to compute the gradients necessary for optimization algorithms, such as stochastic gradient descent or Adam optimizer, to update the network weights and biases during the training process.

8. Training and Optimization: Training the PINN involves minimizing the physics-informed loss function through iterative optimization. This process involves forward propagation, where inputs are passed through the network to obtain predictions, followed by backpropagation, where gradients are calculated to update the network parameters. The training process aims to find the optimal values for the network weights and biases that minimize the loss function and improve the accuracy of the predictions.

9. Hyperparameters: PINNs contain hyperparameters that need to be determined before training the network. These hyperparameters include the learning rate, regularization parameters, number of hidden layers, and the number of neurons in each layer. The selection of these hyperparameters is crucial for achieving optimal performance and preventing issues such as overfitting or underfitting.

The architecture and components of PINNs provide a powerful framework for accurately modelling fluid flow behaviour. By integrating the governing equations of fluid mechanics, PINNs ensure physical consistency in the predictions while leveraging the capabilities of neural networks to capture complex relationships and patterns within the data. This unique combination allows PINNs to overcome the limitations of traditional modelling approaches and offer a data-driven, physics-informed solution for understanding and predicting fluid flow dynamics.

3.2. Applicability of PINNs in modelling non-Newtonian fluids.

Neural networks have emerged as powerful tools in various fields, including fluid mechanics, for modelling and predicting complex phenomena. This section introduces neural networks and highlights their applicability in fluid flow modelling, setting the stage for their integration into the study of fluid mechanics and dynamics (50). Neural networks are a category of machine learning models constructed based on the principles of neuronal organization observed in biological neural networks found in

animal brains, as discovered by connectionism (50). They consist of interconnected nodes, called neurons, organized into layers. These networks can learn from data and capture intricate patterns and relationships that may be difficult to discern through conventional mathematical modelling approaches (24).

In the context of fluid flow modelling, neural networks offer several advantages. First, they provide a flexible framework capable of approximating highly nonlinear relationships between input and output variables. Traditional mathematical models often rely on linear assumptions and simplifications that may not capture the complexities inherent in fluid flow behaviour. Neural networks can handle the intricate and nonlinear nature of fluid dynamics, making them suitable for a wide range of flow scenarios (23).

Second, neural networks can learn directly from data, allowing for data-driven modelling of fluid flow phenomena (51). This data-driven approach is particularly valuable when experimental or observational data is available, but the underlying governing equations are unknown or difficult to derive. Neural networks can learn the mapping between input data (e.g., flow conditions, geometry, and boundary conditions) and output data (e.g., flow fields, pressure, or velocity profiles), enabling accurate predictions without explicitly formulating the governing equations (28). Moreover, neural networks offer the ability to incorporate prior knowledge and physical constraints into the modelling process. Known physics principles and governing equations can be integrated into the neural network architecture, resulting in what are known as PINNs. By combining data-driven learning with physics-based constraints, PINNs enhance the accuracy and reliability of fluid flow predictions while maintaining physical consistency.

The applicability of neural networks in fluid flow modelling extends to various areas within fluid mechanics. They have been successfully employed in modelling turbulent flows, multiphase flows (52), flow control, heat transfer (53), and more. Neural networks can capture the complex interactions and nonlinearities that arise in these scenarios, providing insights into flow behaviour and supporting the design and optimization of engineering systems.

PINNs integrate the capabilities of neural networks with the governing equations of fluid mechanics, which enables them to capture the underlying physics of fluid flow while leveraging the data-driven capabilities of neural networks. By incorporating the physics equations into the neural network architecture, PINNs ensure that the predicted flow fields satisfy the fundamental laws of fluid dynamics. The advantages of using PINNs for modelling non-Newtonian fluids are as follows:

1. Capturing Complex Non-Newtonian Behaviour: Non-Newtonian fluids exhibit intricate behaviours such as shear thinning, shear thickening, and yield stress effects. Traditional modelling approaches often struggle to accurately capture these complex behaviours. However, PINNs, with their ability to approximate highly nonlinear functions, are well-suited to model the intricate behaviour exhibited by non-Newtonian fluids (26). PINNs can effectively capture and represent the complex flow behaviour that arises from the interactions between stress, strain, and deformation history in non-Newtonian fluids.

2. Integration of Constitutive Models: Non-Newtonian fluid behaviour is typically described by constitutive models that relate stress, strain, and deformation history. PINNs offer a framework to seamlessly integrate these constitutive models as additional physics constraints in the loss function. By incorporating the constitutive equations, PINNs can accurately represent the non-Newtonian behaviour and ensure that the predicted flow fields adhere to the underlying constitutive relationships. This integration enhances the fidelity and accuracy of the modelling process.

3. Mesh-Free and Flexible Framework: Traditional computational fluid dynamics methods often require the generation of structured meshes to discretize the computational domain (42). However, mesh generation can be challenging for complex geometries or evolving flow domains encountered in non-Newtonian fluid flow. PINNs provide a mesh-free and flexible framework, eliminating the need for explicit mesh generation. This flexibility allows for the modelling of complex geometries and non-uniform domains, making PINNs well-suited for accurately predicting the behaviour of non-Newtonian fluids in real-world scenarios.

4. Efficient Training and Prediction: PINNs leverage advanced optimization techniques and automatic differentiation to efficiently train the network and minimize the loss function. The training process involves solving the forward and inverse problems simultaneously, resulting in a more accurate representation of the flow behaviour. Once trained, PINNs can rapidly predict flow fields, enabling real-time simulations and optimization in various engineering and scientific applications. The computational efficiency of PINNs makes them particularly advantageous for complex non-Newtonian fluid flow simulations.

5. Data-Driven Approach: PINNs offer a data-driven approach to modelling non-Newtonian fluid flow. They can assimilate experimental or observational data, enabling the incorporation of real-world information into the modelling process. This data-driven capability enhances the accuracy and reliability of predictions, particularly when experimental data is available but the underlying governing equations are unknown or difficult to derive.

4. Methodology and Setup

4.1. Constitutive models in study.

In this study, two rheological constitutive models are analysed, namely the Carreau-Yasuda model and the Cross Power-Law model.

The Carreau-Yasuda constitutive model belongs to the class of Generalized Newtonian Fluid models, and is specifically designed to characterise the changes in viscosity as a function of shear rate in polymer solutions and melts (26). Apart from the equation as illustrated in Equation 4, the Carreau-Yasuda model can be concisely expressed in terms of viscosity as shown in Equation 6, with a total of five parameters which effectively captures the viscosity limits observed at both high and low frequencies and provides valuable insights into the rheological behaviour of these complex fluid systems.

$$\nu = \nu_\infty + (\nu_0 - \nu_\infty)[1 + (\lambda\dot{\gamma})^a]^{\frac{n-1}{a}} \quad [6]$$

Similar to Equation 4, λ refers to the relaxation time constant, which determines the time scale at which the fluid responds to variations in shear rate. A higher λ value indicates a slower response to shear rate changes, while a lower λ implies a more rapid response. a refers to the power-law index at low shear rates, which accounts for the curvature in the viscosity-shear rate relationship of the fluid. This parameter is associated with the shape of the curve and affects the smoothness of the viscosity transition between low and high shear rates. n refers to the power-law index at high shear rates, which governs the shear-thinning behaviour of the fluid. It determines the rate at which the viscosity decreases with increasing shear rate. A higher n value implies a stronger shear-thinning effect, while a lower n signifies a milder decrease in viscosity with shear rate. In addition, ν_0 refers to the zero-shear viscosity, which characterizes the initial viscosity behaviour of the fluid. ν_∞ refers to the high-shear rate viscosity, which signifies the limiting viscosity of the fluid as the shear rate becomes large or the frequency approaches infinity. In this study, the values of the parameters used in the Carreau-Yasuda model are: $\nu_0 = 10^{-3}$ Pa s, $\nu_\infty = 10^{-5}$ Pa s, $\lambda = 1$, and $n = 0.5$, as illustrated in Table 1.

The Cross Power-Law model is a widely used constitutive equation in the field of rheology to describe the flow behaviour of non-Newtonian fluids. This model incorporates several parameters that govern the relationship between shear stress and shear rate, which enables the characterization of various flow properties. The model is concisely illustrated in terms of viscosity as shown in Equation 5. One important pointer is that the parameter K refers to the flow consistency index, which represents the fluid's resistance to flow when the shear rate is low. This quantifies the material's intrinsic viscosity and provides insight about its overall flow behaviour. Generally, a higher K value signifies a more viscous or resistant fluid, while a lower K values indicates a more easily flowing fluid. In this study, the values of the parameters used in the Cross Power-Law model are: $\nu_0 = 10^{-2}$ Pa s, $\nu_\infty = 10^{-4}$ Pa s, $K = 2$, and $n = 0.3$, as shown in Table 1.

Constitutive Model	ν_0 (Pa s)	ν_∞ (Pa s)	λ	K	n
Carreau-Yasuda	10^{-3}	10^{-5}	1	-	0.5
Cross Power-Law	10^{-2}	10^{-4}	-	2	0.3

Table 1. Parameters of the models used in the study

4.2. Flow Scenarios.

In this study, various flow scenarios and setups are analyzed to comprehensively evaluate the capability of PINNs to generalize its predictive power to different types of flow. Therefore, a total of three distinct flow scenarios are studied, as illustrated below in Figures 3a, 4a, and 5a.

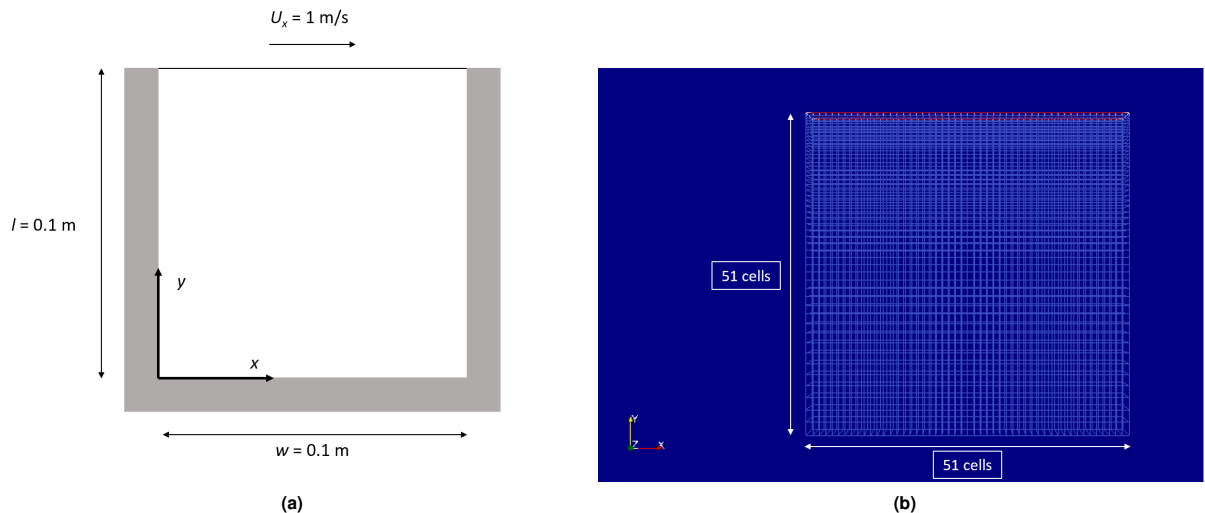


Fig. 3. (a) Geometry, initial and boundary conditions of first flow scenario in study. (b) Mesh generation for 2-dimensional flow domain.

The first flow scenario is likened to a Couette flow (54), as depicted in Figure 3a above. The initial flow within the domain is stationary, while the top wall maintains a constant rightward velocity of 1 m/s and the other walls remain stationary. One important pointer is that there is no initial pressure gradient or difference within the flow domain. The 2-dimensional flow domain has a length of 0.1m and a width of 0.1m, which makes it a square-shaped domain. The simulation is run using OpenFOAM, for a duration of 5.5 seconds with a time-step of 0.025 seconds. The flow domain is discretized into a total of 2061 cells, with 51 cells along the vertical axis and 51 cells along the horizontal axis, as shown in Figure 3b. Fluids belonging to

both the Carreau-Yasuda and Cross Power-Law models, as discussed in the [Constitutive models in study](#) sub-section, are put through this flow scenario in this study.

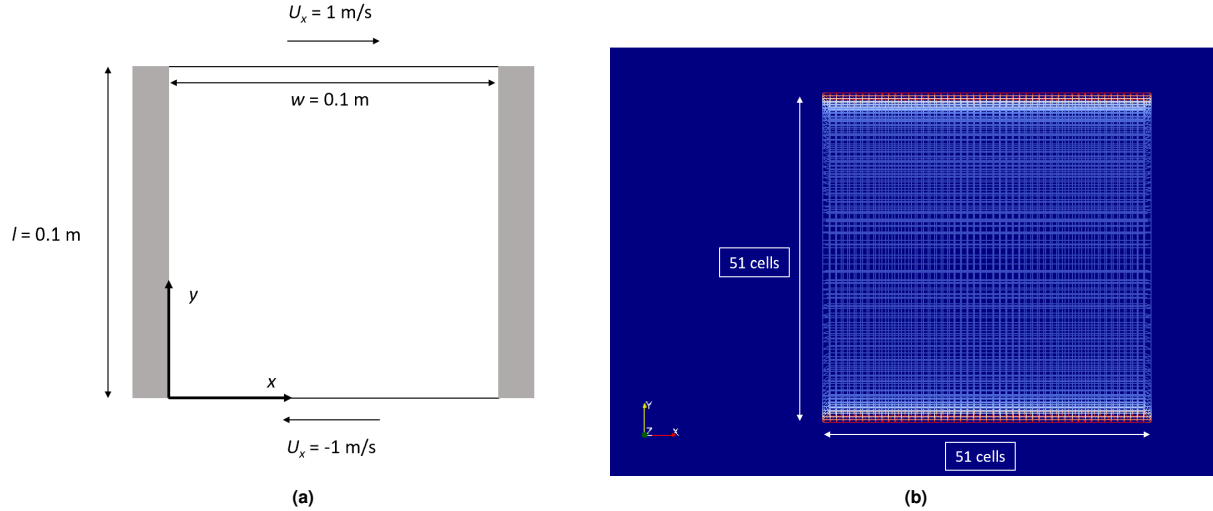


Fig. 4. (a) Geometry, initial and boundary conditions of second flow scenario in study. (b) Mesh generation for 2-dimensional flow domain.

The second flow scenario is depicted in Figure 4a above. The initial flow within the domain is stationary, while the top wall maintains a constant rightward velocity of 1 m/s and the bottom wall maintains a constant opposing leftward velocity of 1 m/s. The left and right walls are kept stationary. One important pointer is that there is no initial pressure gradient or difference within the flow domain. The 2-dimensional flow domain has a length of 0.1m and a width of 0.1m, which makes it a square-shaped domain. The simulation is run using OpenFOAM, for a duration of 5.5 seconds with a time-step of 0.025 seconds. The flow domain is discretized into a total of 2061 cells, with 51 cells along the vertical axis and 51 cells along the horizontal axis, as shown in Figure 4b. Fluids belonging to both the Carreau-Yasuda and Cross Power-Law models, as discussed in the [Constitutive models in study](#) sub-section, are put through this flow scenario in this study.

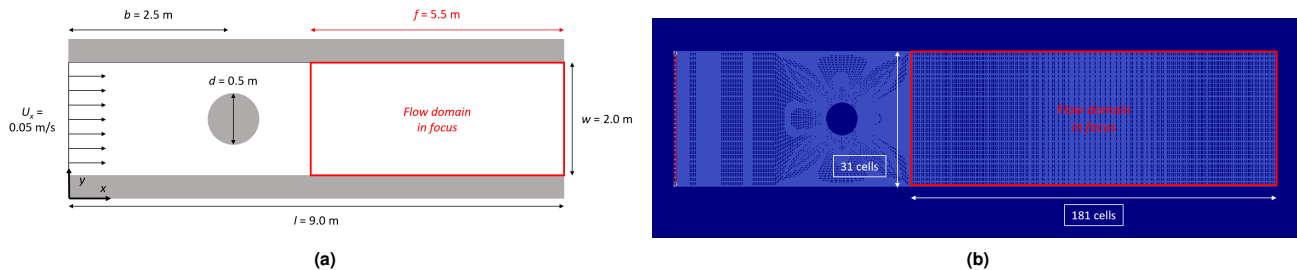


Fig. 5. (a) Geometry, initial and boundary conditions of third flow scenario in study. (b) Mesh generation for 2-dimensional flow domain.

The third flow scenario is basically a non-Newtonian flow over a stationary circular cylinder, as illustrated in Figure 5a above. The initial flow starts from the left boundary and is directed towards the circular cylinder on the right, with a uniform velocity of 0.05 m/s. All the walls are kept stationary. One important pointer is that there is no initial pressure difference or gradient within the flow domain. The 2-dimensional flow domain has a length of 9.0m and a width of 2.0m, which gives it a rectangular shape. The circular cylinder has a diameter of 0.5m. In order to only analyze the region of the flow past the cylinder, the domain in focus refers to the region marked by the red rectangular box, as represented in Figure 5a above. The simulation is run using OpenFOAM, for a duration of 100 seconds with a time-step of 0.5 seconds. The flow domain is discretized into a total of 5611 cells, with 31 cells along the vertical axis and 181 cells along the horizontal axis, as shown in Figure 5b. Fluids belonging to both the Carreau-Yasuda and Cross Power-Law models, as discussed in the [Constitutive models in study](#) sub-section, are put through this flow scenario in this study.

For more convenient reference and simpler representation, the flow protocols discussed in this study are concisely denoted (26) in Table 2 below. There are a total of six flow protocols, and they shall be referred to by their code (e.g., 1A, 1B etc.) when discussing the findings and results in the Results and Discussion section.

4.3. Building the PINN for non-Newtonian flow modelling.

Building a PINN for predicting non-Newtonian fluid flow involves combining principles of fluid mechanics with neural network

Flow Protocol	Flow Scenario	Constitutive Model
1A	First flow scenario	Carreau-Yasuda model
1B	First flow scenario	Cross Power-Law model
2A	Second flow scenario	Carreau-Yasuda model
2B	Second flow scenario	Cross Power-Law model
3A	Third flow scenario	Carreau-Yasuda model
3B	Third flow scenario	Cross Power-Law model

Table 2. Flow protocols discussed in study

architectures to create a data-driven model that incorporates physical laws and constraints. Machine learning frameworks can be divided into two broad categories based on the available data: supervised learning and unsupervised learning (55). Within the field of supervised machine learning, neural networks form a subset of algorithms that establish correlations between inputs and outputs, constructing a computational data-driven framework. This is accomplished by optimizing the variables of the neurons to minimize the difference between the predicted and actual data (26). As traditional neural networks rely solely on statistical considerations during the training process, this results in predictions from these networks lacking significant consideration for physical laws governing fluid flow. In this study, non-linear physical governing laws are directly incorporated into the neural network architecture. These governing laws refer to the 2-dimensional Navier-Stokes equations, as shown below in Equations 7, 8 and 9.

Continuity equation:

$$\frac{\partial u}{\partial x} + \frac{\partial v}{\partial y} = 0 \quad [7]$$

x-Momentum equation:

$$\frac{\partial u}{\partial t} + u \frac{\partial u}{\partial x} + v \frac{\partial u}{\partial y} = -\frac{1}{\rho} \frac{\partial P}{\partial x} + \nu \left(\frac{\partial^2 u}{\partial x^2} + \frac{\partial^2 u}{\partial y^2} \right) \quad [8]$$

y-Momentum equation:

$$\frac{\partial v}{\partial t} + u \frac{\partial v}{\partial x} + v \frac{\partial v}{\partial y} = -\frac{1}{\rho} \frac{\partial P}{\partial y} + \nu \left(\frac{\partial^2 v}{\partial x^2} + \frac{\partial^2 v}{\partial y^2} \right) \quad [9]$$

Automatic Differentiation (56), also known as algorithmic differentiation, is utilized to integrate the Navier-Stokes equations into the PINN framework. It is a computational technique used to evaluate derivatives of mathematical functions with respect to their input variables, and provides an efficient and accurate way to compute gradients, which are essential in sensitivity analysis, optimization, and machine learning algorithms (57). By using Automatic Differentiation, differentiation of the neural network can be performed with respect to its input parameters and model parameters (26). The input parameters refer to the spatial (x , y) and the temporal (t) coordinates. The output parameters refer to the horizontal and vertical velocities (u , v) and pressure outputs (P). These are illustrated in the schematic diagram of the PINN, as illustrated below in Figure 6. Subsequently, the cumulative loss function, which is the sum of the loss from the initial and boundary conditions and the loss from the physical governing equations, is computed using the outputs of the neural network.

To calculate the loss from the governing equations, it is important to first define the residuals of the system of Navier-Stokes equations. The residuals are defined as F_1 , F_2 and F_3 , in terms of components of the stress tensor, as illustrated in Equations 10, 11 and 12.

F_1 residual:

$$F_1(x, y, t) = \frac{\partial u}{\partial x} + \frac{\partial v}{\partial y} \quad [10]$$

F_2 residual:

$$F_2(x, y, t) = \frac{\partial u}{\partial t} + u \frac{\partial u}{\partial x} + v \frac{\partial u}{\partial y} + \frac{1}{\rho} \frac{\partial P}{\partial x} + \frac{1}{\rho} \left(\frac{\partial \sigma_{xx}}{\partial x} + \frac{\partial \sigma_{xy}}{\partial y} \right) \quad [11]$$

F_3 residual:

$$F_3(x, y, t) = \frac{\partial v}{\partial t} + u \frac{\partial v}{\partial x} + v \frac{\partial v}{\partial y} + \frac{1}{\rho} \frac{\partial P}{\partial y} + \frac{1}{\rho} \left(\frac{\partial \sigma_{yx}}{\partial x} + \frac{\partial \sigma_{yy}}{\partial y} \right) \quad [12]$$

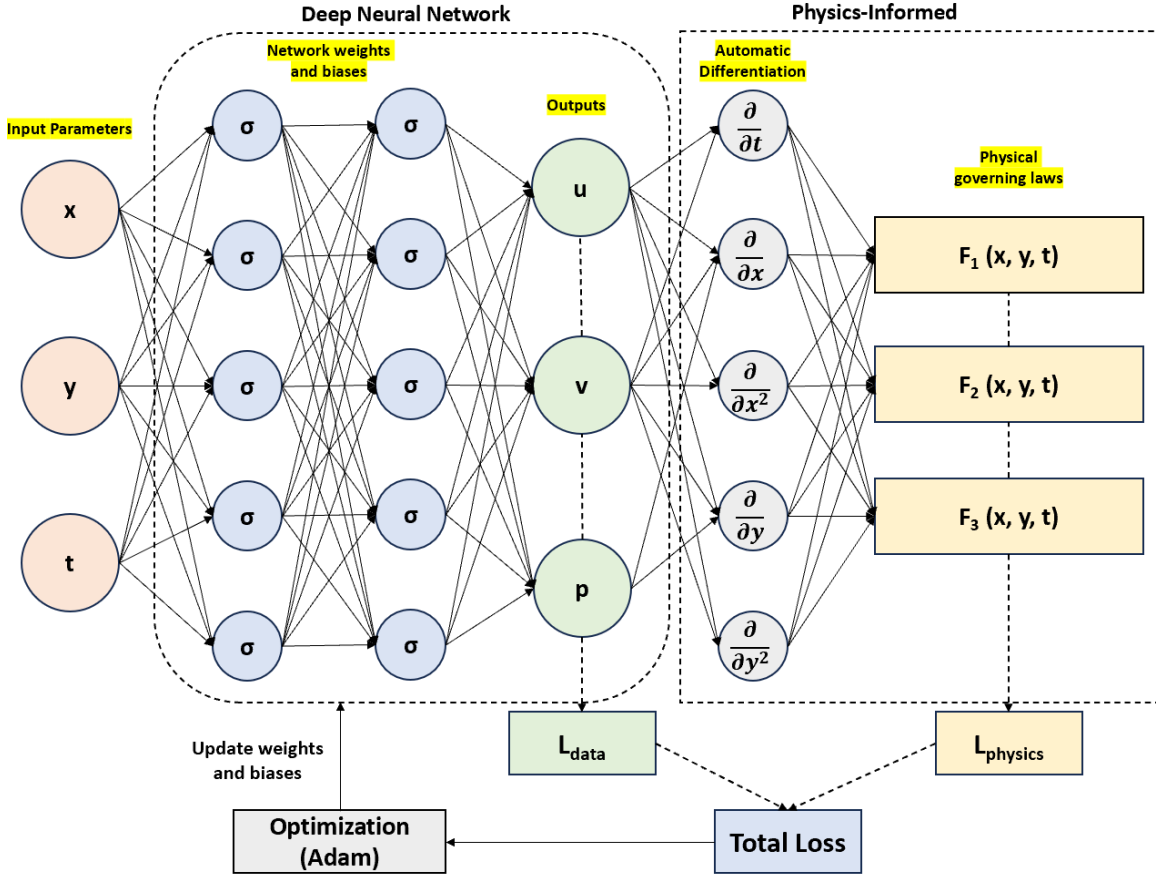


Fig. 6. Architecture of the Physics-informed neural network designed to model non-Newtonian fluid flow in this study. The total loss is computed through the sum of the loss from the data (L_{data}), including losses from the initial and boundary conditions, and the loss from the governing Navier-Stokes equations ($L_{physics}$). Adam optimizer is utilized in this PINN to update the weights and biases of the network during the training phase.

As shown in the architecture of the PINN in Figure 6, the PINN comprises a deep neural network and a "physics-informed" structure. Similar to traditional neural networks, the deep neural network is trained on training data and subsequently tested on testing data. Both the training and testing data are obtained through an open source visualization application (ParaView), by conducting the simulations as described in the [Flow Scenarios](#) sub-section. The training data are derived only from the initial and boundary conditions, in order to ensure fair evaluation and reliable performance estimation of the network. The deep neural network consists of a total of 7 hidden layers with 20 hidden neurons in each layer. In addition to the deep neural network, the "physics-informed" structure introduces the utilization of physical equations to govern the training procedure. Therefore, the weights and biases of the network, which are parameters that determine the performance and behaviour of the network during the training process (58), are machine-learned through the minimization of the loss function. The total loss function (shown in Equation 15) can be mainly summarized as the combination of two components: the sum of the residuals F_1 , F_2 and F_3 , also known as the loss based on the physical law (shown in Equation 13), as well as the loss due to the difference between the actual and predicted initial and boundary conditions (26) (shown in Equation 14).

Loss based on physical law:

$$MSE_f = \frac{1}{N_f} \sum_{i=1}^{N_f} \left(|F_1(x^i, y^i, t^i)|^2 + |F_2(x^i, y^i, t^i)|^2 + |F_3(x^i, y^i, t^i)|^2 \right) \quad [13]$$

In Equation 13, N_u refers to the number of collocation points within the domain from which the data was retrieved, in order to compute the mean-squared error for the residuals.

Loss due to initial and boundary conditions:

$$MSE_u = \frac{1}{N_u} \sum_{i=1}^{N_u} \left(|u(x^i, y^i, t^i) - u^i|^2 + |v(x^i, y^i, t^i) - v^i|^2 + |p(x^i, y^i, t^i) - p^i|^2 \right) \quad [14]$$

In Equation 14, N_f refers to the number of collocation points within the domain from the initial and boundary conditions, where the data was retrieved, in order to compute the mean-squared error for the loss due to initial and boundary conditions. $u(x^i, y^i, t^i)$ and u^i refer to the actual and predicted values of the horizontal velocity component respectively, $v(x^i, y^i, t^i)$ and v^i refer to the actual and predicted values of the vertical velocity component respectively, while $p(x^i, y^i, t^i)$ and p^i refer to the actual and predicted values of pressure.

Total Loss:

$$MSE = MSE_f + MSE_u \quad [15]$$

In order to minimize the total loss for a reasonable performance of the PINN, there are two distinct options to terminate the training process. The first option is to allow the network to iterate through a specific number of training epochs (time-based), while the second option is to allow the network to train until the total loss becomes smaller than a certain threshold level (loss-based). In this study, the first option is utilized, and the training process is terminated after a total of 1000 training epochs. Through the 1000 epochs, the network weights and biases are updated continuously, which results in a general decrease in the training loss and an overall increase in the prediction accuracy. In addition, the Adam optimizer is employed for the optimization process during the training phase. This is mainly due to its effectiveness in training deep neural networks, its adaptability to varying learning rates, and its ability to handle large datasets (59).

5. Results and Discussion

In this section, the results obtained from the physics-informed neural network (PINN) predictions will be presented, analyzed and compared against the experimental data obtained from conducting fluid flow simulation using OpenFOAM. The main aim is to assess the performance and accuracy of the PINN model in capturing the complex non-Newtonian fluid behavior in the different scenarios described in the [Flow Scenarios](#) sub-section, specifically in relation to available experimental measurements. To perform a comprehensive analysis of the results, both the qualitative and quantitative aspects will be focused on. Qualitatively, a detailed visual comparison using the flow domain diagrams will be performed between the predicted and actual data, where similarities, differences and any notable features or patterns will be identified. Quantitatively, the accuracy of the PINN predictions will be evaluated by studying the numerical discrepancy or error between the predicted and actual solutions. As there are a total of six different flow protocols, each protocol's results will be separately discussed in their own sub-sections. The plots for the loss against the training epochs for training of the PINNs for all the flow protocols are illustrated in Figures [7a](#), [7b](#), [8a](#), [8b](#), [9a](#), and [9b](#) below.

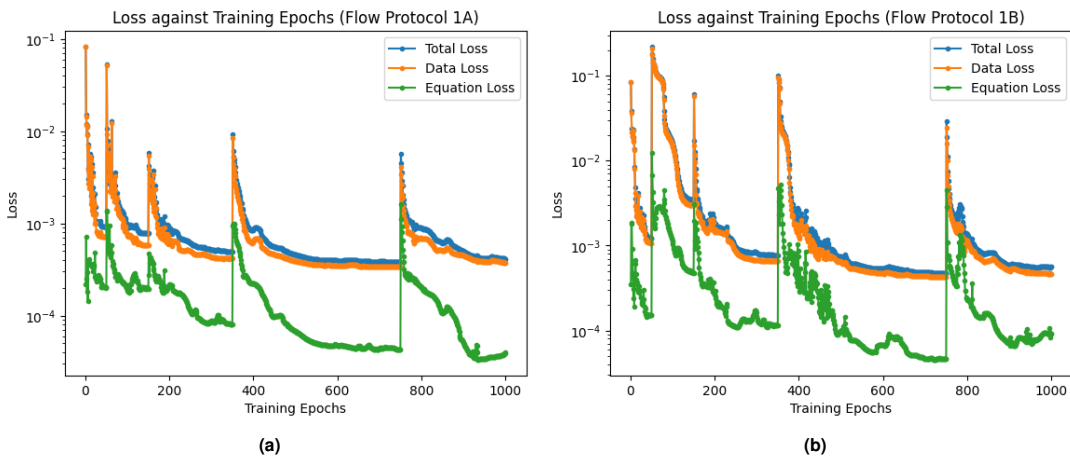


Fig. 7. (a) Plot of loss against training epochs for Flow Protocol 1A. **(b)** Plot of loss against training epochs for Flow Protocol 1B. The blue, orange, and green plots refer to the total loss, the loss due to initial and boundary conditions, and the loss based on physical laws respectively.

As evident in the plots of loss against training epochs for all the flow protocols, there are several sharp spikes in the training loss at some epochs. This is due to a learning rate scheduling technique used in the training process of the PINN

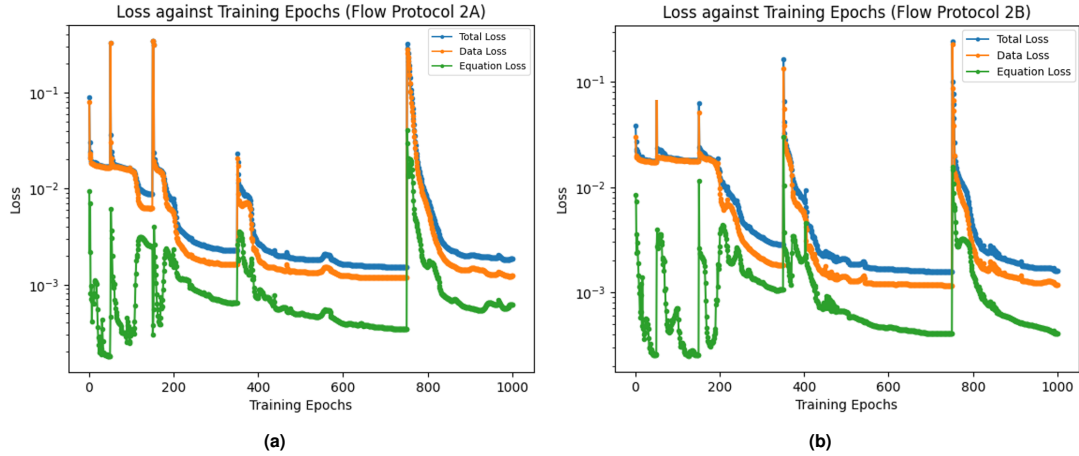


Fig. 8. (a) Plot of loss against training epochs for Flow Protocol 2A. (b) Plot of loss against training epochs for Flow Protocol 2B. The blue, orange, and green plots refer to the total loss, the loss due to initial and boundary conditions, and the loss based on physical laws respectively.

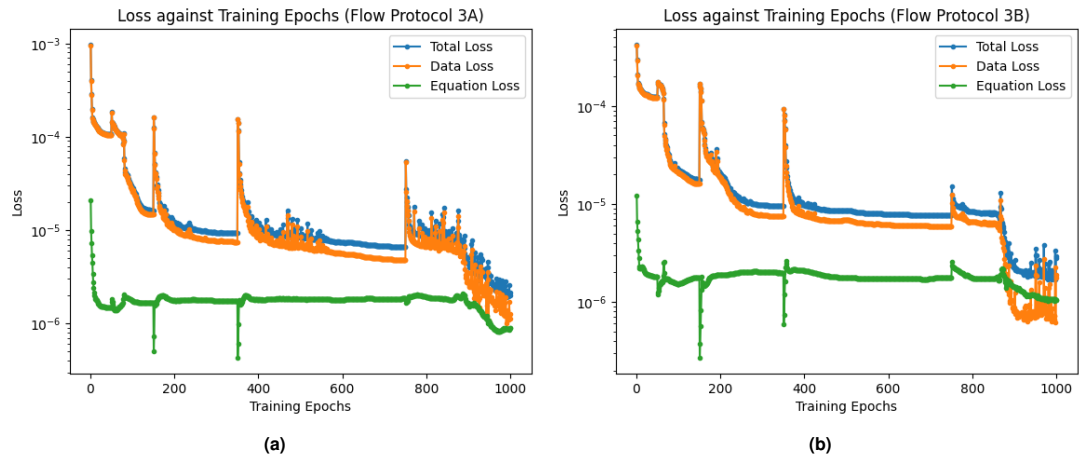


Fig. 9. (a) Plot of loss against training epochs for Flow Protocol 3A. (b) Plot of loss against training epochs for Flow Protocol 3B. The blue, orange, and green plots refer to the total loss, the loss due to initial and boundary conditions, and the loss based on physical laws respectively.

called *CosineAnnealingWarmRestarts* as documented in PyTorch. The purpose of utilizing this technique is to enhance the optimization process during the training of the deep neural network, by dynamically adjusting the learning rate over epochs in a cyclical manner. The concept of cosine annealing comes from the observation that a cyclical learning rate can lead to better optimization by escaping local minima and finding more favorable regions in the loss landscape. The cosine annealing schedule reduces the learning rate in a smooth, periodic manner, resembling the shape of the cosine function (60). Warm restarts are introduced to further improve the optimization process. After completing a cycle of cosine annealing, the learning rate is increased to a higher value, essentially restarting the process. This allows the optimization algorithm to explore different regions of the loss landscape and potentially find better solutions. The combined technique of cosine annealing with warm restarts helps to achieve a balance between exploration and exploitation during training. It provides a regularization effect, preventing the model from getting trapped in local optima and allowing it to converge to better global optima.

5.1. Results for Flow Protocols 1A and 1B.

In order to qualitatively evaluate the performance of PINNs in predicting the non-Newtonian fluid flow, it is essential to present a visual representation of the actual and predicted profile of the entire flow domain, as well as the discrepancy between both profiles. For Flow Protocols 1A and 1B, only the horizontal velocity (u) profile of the domain will be presented and discussed, as the vertical velocity (v) and pressure (p) values are insignificant and therefore negligible, in the case of these specific flow protocols. For Flow Protocol 1A, the horizontal velocity profiles for the entire flow domain at specific timestamps ($t = 1.1\text{s}$, 2.2s , 3.3s , 4.4s , and 5.5s) are illustrated in Figure 10 in the [Appendix](#) section.

In Figure 10, for the discrepancy plots in the right column, the red regions represent points whereby the predicted velocity value is greater than the actual velocity value (over-predict) while the blue regions represent points whereby the predicted velocity value is smaller than the actual velocity value (under-predict). The green and turquoise regions represent regions

where the predicted values are similar to the actual values, and intuitively, these regions should be dominant to illustrate that the PINN is highly accurate. From Figure 10, it is evident that the prediction of the velocity profile closely follows the ground-truth velocity profile. However, there is under-prediction of the velocity near the right boundary of the domain (dark blue region) and over-prediction of the velocity near the bottom wall of the domain (red region), as shown in the discrepancy plots. In addition, from Figure 11a, for the first 0.3 seconds, there is a noticeable under-prediction of the flow velocity by a magnitude of 0.10 - 0.15m/s, which occurs at the region near the moving top wall. Overall, quantitative comparison of the whole domain across the entire duration gives an average prediction error of 1.2%.

However, the visual description in Figure 10 might not be representative of the entire duration of the flow protocol. Therefore, the actual velocity profile at the mid-section of the flow domain (specifically at $x = 0.05\text{m}$) is plotted against time, and compared with the predicted velocity profile obtained from the PINN, as shown in Figures 11b and 11c. From Figures 11b and 11c, it is evident that the predicted velocity profile closely follows the ground-truth profile. This is supported by the discrepancy plot in Figure 11d, which shows that there are largely insignificant differences (turquoise regions) between the actual and predicted velocity profiles, except for some slight discrepancies (blue and yellow regions) between $t = 0\text{s}$ and $t = 20\text{s}$.

For Flow Protocol 1B, the horizontal velocity profiles for the entire flow domain at specific timestamps ($t = 1.1\text{s}, 2.2\text{s}, 3.3\text{s}, 4.4\text{s}$, and 5.5s) are illustrated in Figure 12 in the [Appendix](#) section. From Figure 12, it is evident that the prediction of the velocity profile closely follows the ground-truth velocity profile. However, similar to Flow Protocol 1A, there is under-prediction of the velocity near the right boundary of the domain (dark blue region) and over-prediction of the velocity near the bottom wall of the domain (red region), as shown in the discrepancy plots. In addition, from Figure 13a, for the first 0.225 seconds, there is a noticeable under-prediction of the flow velocity by a magnitude of 0.10 - 0.22m/s, which occurs at the region near the moving top wall. Overall quantitative comparison of the whole domain across the entire duration gives an average prediction error of 1.5%. The actual velocity profile at the mid-section of the flow domain (specifically along $x = 0.05\text{m}$) is plotted against time, and compared with the predicted velocity profile obtained from the PINN, as shown in Figures 13b and 13c. From Figures 13b and 13c, it is evident that the predicted velocity profile closely follows the ground-truth profile. This is supported by the discrepancy plot in Figure 13d, which shows that there are largely insignificant differences (turquoise regions) between the actual and predicted velocity profiles, except for some slight discrepancies (orange and yellow regions) between $t = 0\text{s}$ and $t = 15\text{s}$.

5.2. Results for Flow Protocols 2A and 2B.

For Flow Protocols 2A and 2B, only the horizontal velocity (u) profile of the domain will be presented and discussed, as the vertical velocity (v) and pressure (p) values are insignificant and therefore negligible, in the case of these specific flow protocols.

For Flow Protocol 2A, the horizontal velocity profiles for the entire flow domain at specific timestamps ($t = 1.1\text{s}, 2.2\text{s}, 3.3\text{s}, 4.4\text{s}$, and 5.5s) are illustrated in Figure 14 in the [Appendix](#) section. From Figure 14, it is evident that the prediction of the velocity profile closely follows the ground-truth velocity profile. However, there is under-prediction of the velocity near the bottom wall of the domain (dark blue region) and over-prediction of the velocity near the left and right boundaries of the domain (red region), as shown in the discrepancy plots. In addition, from Figure 15a, for the first 0.6 seconds, there is an observable under-prediction of the flow velocity by a magnitude of 0.16 - 0.26m/s, which occurs at the regions near the top and bottom walls. Overall, quantitative comparison of the whole domain across the entire duration gives an average prediction error of 3.2%. The actual velocity profile at the mid-section of the flow domain (specifically at $x = 0.05\text{m}$) is plotted against time, and compared with the predicted velocity profile obtained from the PINN, as shown in Figures 15b and 15c. From Figures 15b and 15c, it is evident that the predicted velocity profile closely follows the ground-truth profile. This is supported by the discrepancy plot in Figure 15d, which shows that there are largely insignificant differences (green regions) between the actual and predicted velocity profiles, except for some slight discrepancies (red and orange regions) between $t = 0\text{s}$ and $t = 25\text{s}$.

For Flow Protocol 2B, the horizontal velocity profiles for the entire flow domain at specific timestamps ($t = 1.1\text{s}, 2.2\text{s}, 3.3\text{s}, 4.4\text{s}$, and 5.5s) are illustrated in Figure 16 in the [Appendix](#) section. From Figure 16, it is evident that the prediction of the velocity profile closely follows the ground-truth velocity profile. However, there is both simultaneous under-prediction and over-prediction of the velocity near the left and right boundaries of the domain (dark blue and red regions), as shown in the discrepancy plots. Furthermore, from Figure 17a, for the first 0.85 seconds, there is an observable over-prediction of the flow velocity by a magnitude of 0.1 - 0.25m/s, which occurs at the regions near the moving top wall. Overall, quantitative comparison of the whole domain across the entire duration gives an average prediction error of 3.4%. The actual velocity profile at the mid-section of the flow domain (specifically at $x = 0.05\text{m}$) is plotted against time, and compared with the predicted velocity profile obtained from the PINN, as shown in Figures 17b and 17c. From Figures 17b and 17c, it is evident that the predicted velocity profile closely follows the ground-truth profile. This is supported by the discrepancy plot in Figure 17d, which shows that there are largely insignificant differences (green regions) between the actual and predicted velocity profiles, except for some slight discrepancies (blue, red and yellow regions) between $t = 0\text{s}$ and $t = 10\text{s}$.

5.3. Results for Flow Protocols 3A and 3B.

For Flow Protocols 3A and 3B, the horizontal velocity (u), vertical velocity (v) and pressure (p) profile of the domain will be presented and discussed.

For Flow Protocol 3A, the horizontal velocity profiles for the entire flow domain at specific timestamps ($t = 20\text{s}, 40\text{s}, 60\text{s}, 80\text{s}$, and 100s) are illustrated in Figure 18 in the [Appendix](#) section. From Figure 18, we see that although the predicted velocity profile closely follows the actual velocity profile, there are some noticeable discrepancies, as seen in the discrepancy plots. At $t = 20\text{s}$ and $t = 40\text{s}$, there is predominant over-prediction of the fluid velocity by an average magnitude of 0.002m/s at the

top wall, as represented by the dark red regions in the flow domain. At $t = 60$ s, $t = 80$ s and $t = 100$ s, there is dominant under-prediction of the fluid velocity by an average magnitude of 0.003m/s along the mid-span of the flow, as represented by the dark blue regions in the flow domain. In addition, from Figure 19a, for the first 11.5 seconds, there is an observable under-prediction of the horizontal flow velocity by a magnitude of 0.005 - 0.008m/s, which occurs at the region near the bottom of the domain of interest. Overall, quantitative comparison of the whole domain across the entire duration gives an average prediction error of 4.6%. To provide a quantitative comparison that is representative of the entire duration ($t = 0$ s to 100s) of the flow protocol, a specific region of interest (along $x = 0.40$ m) is selected. The actual horizontal velocity profile at the region of interest of the flow domain (specifically along $x = 0.40$ m) is plotted against time, and compared with the predicted horizontal velocity profile obtained from the PINN, as shown in Figures 19b and 19c. From Figures 19b and 19c, it is evident that the predicted velocity profile closely follows the ground-truth profile. This is supported by the discrepancy plot in Figure 19d, which shows that there are largely insignificant differences (green regions) between the actual and predicted velocity profiles, except for some slight discrepancies (dark blue and red regions) between $t = 0$ s and $t = 3$ s.

For Flow Protocol 3A, the vertical velocity profiles for the entire flow domain at specific timestamps ($t = 20$ s, 40s, 60s, 80s, and 100s) are illustrated in Figure 20 in the [Appendix](#) section. From Figure 20, we see that although the predicted velocity profile closely follows the actual velocity profile, there are some noticeable discrepancies, as observed in the discrepancy plots. At $t = 20$ s, there is predominant under-prediction of the fluid velocity by an average magnitude of 0.001m/s around the entire flow domain, as represented by the dark blue regions in the flow domain. At $t = 40$ s, $t = 60$ s, $t = 80$ s and $t = 100$ s, there is dominant over-prediction of the fluid velocity by an average magnitude of 0.001m/s at the left half of the flow domain, as represented by the dark red regions in the flow domain. In addition, from Figure 21a, for the first 29.5 seconds, there is a detectable over-prediction of the vertical flow velocity by a magnitude of 0.0012 - 0.004m/s, which occurs at the region near the left boundary of the domain of interest. Overall, quantitative comparison of the whole domain across the entire duration gives an average prediction error of 4.4%. To provide a quantitative comparison that is representative of the entire duration ($t = 0$ s to 100s) of the flow protocol, a specific region of interest (along $x = 0.40$ m) is selected. The actual vertical velocity profile at the region of interest of the flow domain (specifically along $x = 0.40$ m) is plotted against time, and compared with the predicted vertical velocity profile obtained from the PINN, as shown in Figures 21b and 21c. From Figures 21b and 21c, it seems that the predicted velocity profile closely follows the ground-truth profile. However, from the discrepancy plot in Figure 21d, we see that there are noticeable differences (orange and dark red regions) between the actual and predicted velocity profiles, which gradually worsens especially from $t = 25$ s and $t = 100$ s.

For Flow Protocol 3A, the actual pressure profile at the region of interest of the flow domain (specifically along $x = 0.40$ m) is plotted against time, and compared with the predicted pressure profile obtained from the PINN, as shown in Figures 22a and 22b. From Figures 22a and 22b, it is evident that the predicted pressure profile closely follows the ground-truth profile. This is supported by the discrepancy plot in Figure 22c, which shows that there are largely insignificant differences (green and yellow regions) between the actual and predicted velocity profiles, except for some slight discrepancies (dark blue and red regions) between $t = 0$ s and $t = 3$ s.

For Flow Protocol 3B, the horizontal velocity profiles for the entire flow domain at specific timestamps ($t = 20$ s, 40s, 60s, 80s, and 100s) are illustrated in Figure 23 in the [Appendix](#) section. From Figure 23, we see that although the predicted velocity profile closely follows the actual velocity profile, there are some noticeable discrepancies, as observed in the discrepancy plots. At $t = 20$ s, $t = 40$ s and $t = 60$ s, there is predominant over-prediction of the fluid velocity by an average magnitude of 0.001m/s around the entire flow domain, as represented by the dark red regions in the flow domain. As time progresses, at $t = 80$ s and $t = 100$ s, we see that the over-prediction issue improves gradually. Furthermore, from Figure 24a, for the first 30.5 seconds, there is a detectable over-prediction of the horizontal flow velocity by a magnitude of 0.001 - 0.0022m/s, which occurs around the domain of interest. Overall, quantitative comparison of the whole domain across the entire duration gives an average prediction error of 5.2%. To provide a quantitative comparison that is representative of the entire duration ($t = 0$ s to 100s) of the flow protocol, a specific region of interest (along $x = 0.40$ m) is selected. The actual horizontal velocity profile at the region of interest of the flow domain (specifically along $x = 0.40$ m) is plotted against time, and compared with the predicted horizontal velocity profile obtained from the PINN, as shown in Figures 24b and 24c. From Figures 24b and 24c, it is evident that the predicted velocity profile closely follows the ground-truth profile. This is supported by the discrepancy plot in Figure 24d, which shows that there are largely insignificant differences (green regions) between the actual and predicted velocity profiles, except for some slight discrepancies (dark blue and red regions) between $t = 0$ s and $t = 3$ s.

For Flow Protocol 3B, the vertical velocity profiles for the entire flow domain at specific timestamps ($t = 20$ s, 40s, 60s, 80s, and 100s) are illustrated in Figure 25 in the [Appendix](#) section. From Figure 25, we see noticeable discrepancies at $t = 20$ s, $t = 60$ s, $t = 80$ s, and $t = 100$ s. At $t = 20$ s and $t = 60$ s, we see dominant over-prediction of the vertical velocity by a magnitude of 0.001m/s at the left half of the domain, as represented by the red and orange regions. At $t = 80$ s, there is predominant over-prediction of the fluid velocity by an average magnitude of 0.0005m/s around the entire flow domain, as represented by the dark red and orange regions in the flow domain. At $t = 100$ s, we see significant under-prediction of the fluid velocity by an average magnitude of 0.001m/s around the entire flow domain, as represented by the blue regions in the flow domain. In addition, from 26a, for the first 45.5 seconds, there is detectable over-prediction and under-prediction of the vertical flow velocity by a magnitude of 0.001 - 0.0017m/s, which occurs at the region near the left boundary of the domain of interest. Overall, quantitative comparison of the whole domain across the entire duration gives an average prediction error of 4.9%. The actual vertical velocity profile at the region of interest of the flow domain (specifically along $x = 0.40$ m) is plotted against time, and compared with the predicted vertical velocity profile obtained from the PINN, as shown in Figures 26b and 26c.

From Figures 26b and 26c, it seems that the predicted velocity profile closely follows the ground-truth profile. However, from the discrepancy plot in Figure 26d, we see that there are noticeable differences (light orange and blue regions) between the actual and predicted velocity profiles.

For Flow Protocol 3B, the actual pressure profile at the region of interest of the flow domain (specifically along $x = 0.40\text{m}$) is plotted against time, and compared with the predicted pressure profile obtained from the PINN, as shown in Figures 27a and 27b. From Figures 27a and 27b, it is clear that there are significant differences between the predicted pressure profile and the ground-truth pressure profile. This is supported by the discrepancy plot in Figure 27c, which shows that there are largely significant differences (dark blue regions) between the actual and predicted velocity profiles, illustrating under-prediction of the pressure by the PINN for most of the flow duration.

6. Applications and Future Directions

6.1. Potential applications of PINNs in practical engineering settings.

With the significantly accurate performance of PINNs in modelling the flow protocols in this study, it is increasingly evident that the integration of PINNs has the potential to revolutionize the prediction and modeling of non-Newtonian flows in practical engineering and industrial settings. In this section, the wide range of potential applications and the significant impact that PINNs can have on various industries are discussed in detail.

One significant application of PINNs lies in the design and optimization of complex fluid systems. By accurately predicting the behavior of non-Newtonian fluids, engineers can make well-informed decisions regarding system design, fluid flow control, and optimization. PINNs offer a data-driven approach that combines the advantages of physics-based modeling and machine learning. This enables engineers to efficiently explore and evaluate a wide range of design parameters and operational conditions, facilitating the optimization of complex fluid systems.

In the field of process engineering, PINNs can play a crucial role in optimizing manufacturing processes that involve non-Newtonian fluids. By accurately modeling the flow behavior, engineers can optimize process parameters to enhance product quality, reduce energy consumption, and improve overall process efficiency. This has significant implications for industries such as chemical processing, food production, and pharmaceutical manufacturing, leading to substantial cost savings and increased productivity.

PINNs also hold great potential in the realm of material science, particularly in the development and characterization of advanced materials. Non-Newtonian fluids often exhibit complex behavior and unique rheological properties that directly impact material processing and performance. Leveraging the power of PINNs, researchers can gain valuable insights into the flow behavior of these materials and optimize processing conditions to achieve improved material properties.

Moreover, the impact of PINNs extends to areas such as environmental engineering and fluid dynamics. Accurate prediction of non-Newtonian fluid flow behavior is crucial in studying and mitigating environmental hazards like pollutant dispersion, sediment transport, and volcanic flows. PINNs can provide accurate predictions in such scenarios, aiding in the development of effective mitigation strategies and risk assessment techniques.

In industrial settings, PINNs can facilitate real-time monitoring and control of non-Newtonian fluid processes. By combining PINNs with sensor data, engineers can develop efficient control algorithms that ensure desired flow characteristics and optimize process performance. This has significant implications in industries like oil and gas, where accurate control of non-Newtonian flows is vital for efficient fluid extraction and transportation.

The potential impact of PINNs in practical engineering and industrial settings extends beyond the areas mentioned above. Their applicability spans across sectors such as biomedical engineering, geotechnical engineering, and renewable energy, among others. PINNs provide a powerful tool for accurate predictions, optimization, and control of non-Newtonian fluid flow systems, ultimately leading to enhanced performance, cost reduction, and improved efficiency in a wide range of practical applications.

In conclusion, the integration of physics-informed neural networks (PINNs) holds substantial potential for revolutionizing the prediction and modeling of non-Newtonian flows in practical engineering and industrial settings. By leveraging the strengths of physics-based modeling and machine learning, PINNs enable accurate predictions, optimization, and control of complex fluid systems. Their impact spans across diverse industries, offering opportunities for enhanced process design, optimization, material development, environmental analysis, and real-time process control. As researchers continue to explore and refine the application of PINNs, transformative advancements in understanding and utilizing non-Newtonian fluid flows in practical engineering and industrial contexts are anticipated.

6.2. Exploration of future research directions.

The use of PINNs for predicting non-Newtonian flows has demonstrated promising capabilities and potential in the field of fluid mechanics. As researchers continue to explore the applications of PINNs in this domain, it is crucial to identify and investigate future research directions that can further enhance their utility and broaden their scope of application. In this study, the main scope was to address the utilization of PINNs for solving forward problems in steady non-Newtonian fluid flow. For future research, two possible avenues that can be further analyzed include addressing inverse problems using PINNs and modelling non-Newtonian unsteady flows.

One intriguing research direction involves leveraging the capabilities of PINNs to address inverse problems in fluid mechanics. Inverse problems involve inferring the unknown inputs or parameters of a physical model based on observed outputs or measurements. In the context of fluid flow, this could include estimating boundary conditions, viscosity profiles, or other fluid properties from velocity or pressure measurements. Solving inverse problems using PINNs would enable us to extract valuable

information about the underlying flow behavior and physical properties even in scenarios where direct measurements of these parameters are challenging or expensive. To tackle inverse problems with PINNs, researchers can integrate additional data from experiments or simulations into the training process. The PINN can be trained to approximate the inverse mapping from the observed data to the unknown inputs or parameters. Regularization techniques and uncertainty quantification methods can be employed to ensure stability and robustness in the solutions. Addressing the ill-posed nature of inverse problems and exploring ways to improve the uniqueness and accuracy of the inferred parameters will be crucial in this research direction.

Another important research direction involves extending the application of PINNs to model unsteady flows of non-Newtonian fluids. Many practical engineering and industrial scenarios involve time-varying flow behavior, and accurately predicting the dynamics of non-Newtonian fluids under unsteady conditions is essential for optimizing system design and performance. Modeling non-Newtonian unsteady flows using PINNs presents both theoretical and computational challenges. It requires the PINN to capture the temporal evolution of fluid properties and flow characteristics accurately. Future research can explore incorporating time-dependent terms and temporal derivatives into the governing equations to account for unsteady behavior. Development of adaptive strategies that dynamically adjust the PINN architecture during the training process can further enhance its capacity to model time-varying phenomena.

7. Conclusion

In this study, a data-driven framework, for predicting a range of different flow scenarios for non-Newtonian fluids governed by the Carreau-Yasuda and Cross Power-Law constitutive models, was presented and evaluated based on its qualitative and quantitative performance against ground-truth solutions derived through OpenFOAM simulation. The primary objectives of this research were to explore the application of PINNs for predicting non-Newtonian flows and to investigate their potential in practical engineering and industrial settings. In addition, the study aimed to leverage on the strengths of PINNs, combining machine learning and physics-based modelling, to accurately predict the complex behavior of non-Newtonian fluids under various flow conditions.

To achieve these objectives, a comprehensive background on non-Newtonian fluids and their complex flow behavior was first introduced. In addition, the challenges associated with modeling these fluids, such as the presence of shear-thinning and shear-thickening behavior, thixotropy, and memory effects, were discussed in detail. The limitations of traditional modeling approaches in capturing the intricate flow characteristics of non-Newtonian fluids were also highlighted. Furthermore, the concept of PINNs and their advantages for modeling non-Newtonian fluid flow were elucidated, together with the incorporation of conservation laws and governing equations into the neural network framework through utilization of Automatic Differentiation. PINNs were recognized for their potential to overcome the limitations of traditional approaches and their ability to efficiently handle complex flow systems with uncertain boundary conditions.

Through rigorous simulations and validation studies, the effectiveness of PINNs in accurately predicting the behavior of non-Newtonian fluids was demonstrated. Overall, comparisons with experimental data and existing numerical simulations revealed the high accuracy and reliability of PINNs in predicting non-Newtonian flows. Lastly, future research directions that can further enhance the capabilities of PINNs in the context of non-Newtonian fluid flow modeling were defined, which included addressing inverse problems using PINNs for parameter estimation and modeling non-Newtonian unsteady flows to capture time-dependent flow behavior.

ACKNOWLEDGMENTS. I would like to thank Dr. Zhu Lai Lai for his valuable feedback and guidance on the topics discussed in the manuscript. Finally, I would like to thank my family for their unwavering support throughout this research.

8. References

1. HF George, F Qureshi, *Newton's Law of Viscosity, Newtonian and Non-Newtonian Fluids*, eds. QJ Wang, YW Chung. (Springer US, Boston, MA), pp. 2416–2420 (2013).
2. RP Chhabra, Non-newtonian fluids: an introduction. *Rheol. complex fluids* pp. 3–34 (2010).
3. MM Cross, Rheology of non-newtonian fluids: a new flow equation for pseudoplastic systems. *J. colloid science* **20**, 417–437 (1965).
4. A Poslinski, M Ryan, R Gupta, S Seshadri, F Frechette, Rheological behavior of filled polymeric systems i. yield stress and shear-thinning effects. *J. Rheol.* **32**, 703–735 (1988).
5. M Wei, K Lin, L Sun, Shear thickening fluids and their applications. *Mater. & Des.* **216**, 110570 (2022).
6. VSR Krishna, S Hussain, CR Kiran, KV Kumar, Experimental evaluation of impact energy on obleck material (non-newtonian fluid). *Mater. Today: Proc.* **45**, 3609–3617 (2021).
7. H Zhu, Y Kim, D De Kee, Non-newtonian fluids with a yield stress. *J. Non-Newtonian Fluid Mech.* **129**, 177–181 (2005).
8. EC Bingham, *An investigation of the laws of plastic flow*. (US Government Printing Office) No. 278, (1917).
9. EC Bingham, *Fluidity and plasticity*. (McGraw-Hill), (1922).
10. JF Steffe, *Rheological methods in food process engineering*. (Freeman press), (1996).
11. Flow properties of polymers (2023) [Online; accessed July 11, 2023].
12. N Phan-Thien, N Mai-Duy, *Understanding viscoelasticity: an introduction to rheology*. (Springer), (2013).
13. RR Huigol, N Phan-Thien, *Fluid mechanics of viscoelasticity: general principles, constitutive modelling, analytical and numerical techniques*. (Elsevier), (1997).
14. PR de Souza Mendes, Modeling the thixotropic behavior of structured fluids. *J. Non-Newtonian Fluid Mech.* **164**, 66–75 (2009).
15. RP Chhabra, JF Richardson, *Non-Newtonian flow in the process industries: fundamentals and engineering applications*. (Butterworth-Heinemann), (1999).
16. BM Johnston, PR Johnston, S Corney, D Kilpatrick, Non-newtonian blood flow in human right coronary arteries: steady state simulations. *J. biomechanics* **37**, 709–720 (2004).
17. RP Chhabra, JF Richardson, *Non-Newtonian flow and applied rheology: engineering applications*. (Butterworth-Heinemann), (2011).
18. T Yan, et al., A novel predictive model of drag coefficient and settling velocity of drill cuttings in non-newtonian drilling fluids. *Petroleum Sci.* **18**, 1729–1738 (2021).
19. M Sorgun, M Ozbayoglu, Predicting frictional pressure loss during horizontal drilling for non-newtonian fluids. *Energy Sources, Part A: Recover. Util. Environ. Eff.* **33**, 631–640 (2011).
20. E Brujan, *Cavitation in Non-Newtonian fluids: with biomedical and bioengineering applications*. (Springer Science & Business Media), (2010).
21. N Balmforth, R Craster, Geophysical aspects of non-newtonian fluid mechanics. *Geomorphol. Fluid Mech.* pp. 34–51 (2001).
22. ME Mackay, The importance of rheological behavior in the additive manufacturing technique material extrusion. *J. Rheol.* **62**, 1549–1561 (2018).
23. M Raissi, P Perdikaris, GE Karniadakis, Physics-informed neural networks: A deep learning framework for solving forward and inverse problems involving nonlinear partial differential equations. *J. Comput. physics* **378**, 686–707 (2019).
24. JA Anderson, *An introduction to neural networks*. (MIT press), (1995).
25. M Raissi, A Yazdani, GE Karniadakis, Hidden fluid mechanics: A navier-stokes informed deep learning framework for assimilating flow visualization data. *arXiv preprint arXiv:1808.04327* (2018).

26. M Mahmoudabadbozchelou, GE Karniadakis, S Jamali, nn-pinns: Non-newtonian physics-informed neural networks for complex fluid modeling. *Soft Matter* **18**, 172–185 (2022).
27. FF de la Mata, A Gijón, M Molina-Solana, J Gómez-Romero, Physics-informed neural networks for data-driven simulation: Advantages, limitations, and opportunities. *Phys. A: Stat. Mech. its Appl.* **610**, 128415 (2023).
28. S Cai, Z Mao, Z Wang, M Yin, GE Karniadakis, Physics-informed neural networks (pinns) for fluid mechanics: A review. *Acta Mech. Sinica* **37**, 1727–1738 (2021).
29. S Cuomo, et al., Scientific machine learning through physics-informed neural networks: Where we are and what's next. *J. Sci. Comput.* **92**, 88 (2022).
30. A Vázquez-Quesada, RI Tanner, M Ellero, Shear thinning of noncolloidal suspensions. *Phys. review letters* **117**, 108001 (2016).
31. SM Al-Zahrani, A generalized rheological model for shear thinning fluids. *J. Petroleum Sci. Eng.* **17**, 211–215 (1997).
32. W Xue, GS Grest, Shear-induced alignment of colloidal particles in the presence of a shear flow. *Phys. review letters* **64**, 419 (1990).
33. E Errill, Rheology of blood. *Physiol. reviews* **49**, 863–888 (1969).
34. NJ Wagner, JF Brady, Shear thickening in colloidal dispersions. *Phys. Today* **62**, 27–32 (2009).
35. YS Lee, NJ Wagner, Dynamic properties of shear thickening colloidal suspensions. *Rheol. acta* **42**, 199–208 (2003).
36. C Clavaud, A Bérut, B Metzger, Y Forterre, Revealing the frictional transition in shear-thickening suspensions. *Proc. Natl. Acad. Sci.* **114**, 5147–5152 (2017).
37. IM Krieger, TJ Dougherty, A mechanism for non-newtonian flow in suspensions of rigid spheres. *Transactions Soc. Rheol.* **3**, 137–152 (1959).
38. BH Manukonda, et al., Rheology based design of shear thickening fluid for soft body armor applications. *Period. Polytech. Chem. Eng.* **64**, 75–84 (2020).
39. JM Brader, Nonlinear rheology of colloidal dispersions. *J. Physics: Condens. Matter* **22**, 363101 (2010).
40. HS Tang, DM Kalyon, Estimation of the parameters of herschel-bulkley fluid under wall slip using a combination of capillary and squeeze flow viscometers. *Rheol. acta* **43**, 80–88 (2004).
41. B Blocken, Computational fluid dynamics for urban physics: Importance, scales, possibilities, limitations and ten tips and tricks towards accurate and reliable simulations. *Build. Environ.* **91**, 219–245 (2015).
42. JR Manson, G Pender, SG Wallis, Limitations of traditional finite volume discretizations for unsteady computational fluid dynamics. *AIAA journal* **34**, 1074–1076 (1996).
43. D Svozil, V Kvasnicka, J Pospichal, Introduction to multi-layer feed-forward neural networks. *Chemom. intelligent laboratory systems* **39**, 43–62 (1997).
44. S Albawi, TA Mohammed, S Al-Zawi, Understanding of a convolutional neural network in 2017 international conference on engineering and technology (ICET). (Ieee), pp. 1–6 (2017).
45. H Salehinejad, S Sankar, J Barfett, E Colak, S Valaee, Recent advances in recurrent neural networks. *arXiv preprint arXiv:1801.01078* (2017).
46. R Miikkulainen, et al., Evolving deep neural networks in *Artificial intelligence in the age of neural networks and brain computing*. (Elsevier), pp. 293–312 (2019).
47. B Ding, H Qian, J Zhou, Activation functions and their characteristics in deep neural networks in 2018 Chinese control and decision conference (CCDC). (Ieee), pp. 1836–1841 (2018).
48. T de Wolff, H Carrillo, L Martí, N Sanchez-Pi, Assessing physics informed neural networks in ocean modelling and climate change applications in AI: Modeling Oceans and Climate Change Workshop at ICLR 2021. (2021).
49. LB Rall, GF Corliss, An introduction to automatic differentiation. *Comput. Differ. Tech. Appl. Tools* **89**, 1–18 (1996).
50. A Brahma, *Comprehensive biomedical physics*. (Newnes), (2014).
51. M Cheng, F Fang, CC Pain, I Navon, Data-driven modelling of nonlinear spatio-temporal fluid flows using a deep convolutional generative adversarial network. *Comput. Methods Appl. Mech. Eng.* **365**, 113000 (2020).
52. E Haghighat, D Amini, R Juanes, Physics-informed neural network simulation of multiphase poroelasticity using stress-split sequential training. *Comput. Methods Appl. Mech. Eng.* **397**, 115141 (2022).
53. R Laubscher, Simulation of multi-species flow and heat transfer using physics-informed neural networks. *Phys. Fluids* **33** (2021).
54. RJ Donnelly, Taylor-couette flow: The early days. *Phys. Today* **44**, 32–39 (1991).
55. SL Brunton, BR Noack, P Koumoutsakos, Machine learning for fluid mechanics. *Annu. review fluid mechanics* **52**, 477–508 (2020).
56. AG Baydin, BA Pearlmutter, AA Radul, JM Siskind, Automatic differentiation in machine learning: a survey. *J. Machine Learn. Res.* **18**, 1–43 (2018).
57. CC Margossian, A review of automatic differentiation and its efficient implementation. *Wiley interdisciplinary reviews: data mining knowledge discovery* **9**, e1305 (2019).
58. A Zayegh, N Al Bassam, Neural network principles and applications. *Digit. systems* (2018).
59. Z Zhang, Improved adam optimizer for deep neural networks in 2018 IEEE/ACM 26th international symposium on quality of service (IWQoS). (Ieee), pp. 1–2 (2018).
60. JK Eshraghian, C Lamme, MR Azghadi, WD Lu, Navigating local minima in quantized spiking neural networks in 2022 IEEE 4th International Conference on Artificial Intelligence Circuits and Systems (AICAS). (IEEE), pp. 352–355 (2022).

9. Appendix

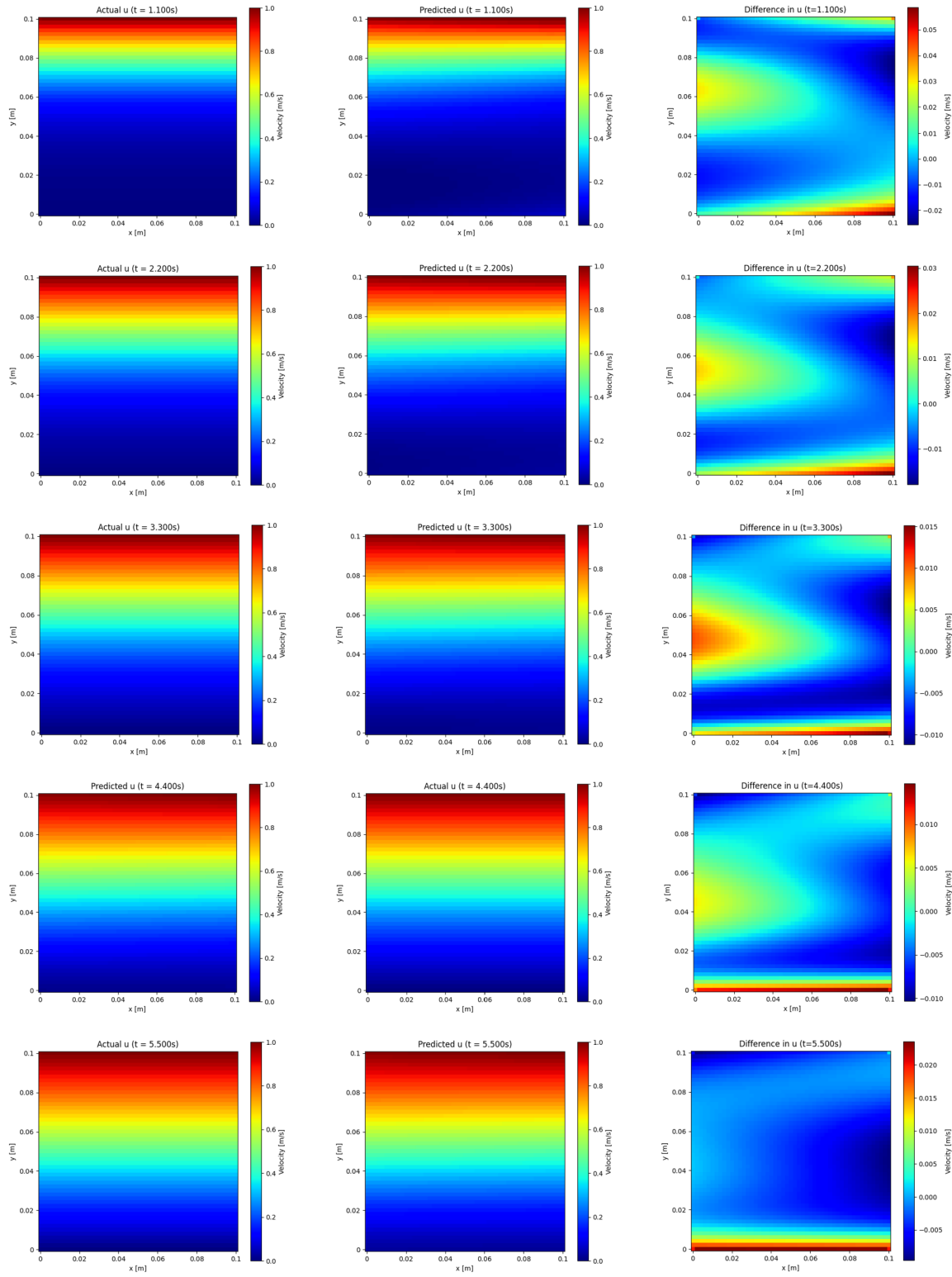


Fig. 10. Horizontal velocity profiles for the whole flow domain at $t = 1.1s, 2.2s, 3.3s, 4.4s$, and $5.5s$. The left column represents the actual velocity profiles, the middle column represents the predicted velocity profiles, and the right column represents the discrepancy between both profiles. These velocity profiles are derived from Flow Protocol 1A.

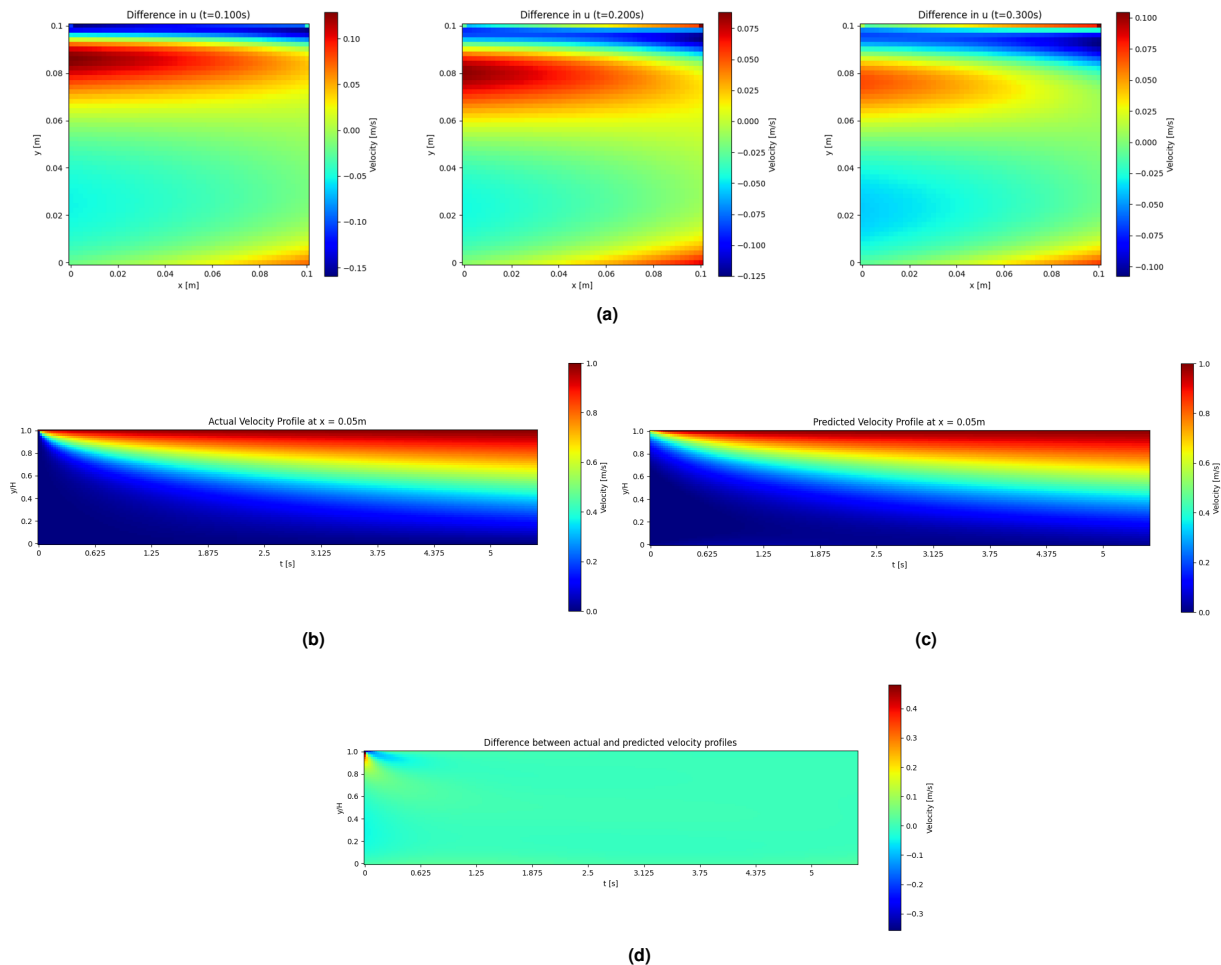


Fig. 11. (a) Discrepancy between actual and predicted horizontal velocity profiles for $t = 0.1\text{s}$, 0.2s , and 0.3s . (b) Actual velocity profile for entire flow duration at mid-section of domain ($x = 0.05\text{m}$). (c) Predicted velocity profile for entire flow duration at mid-section of domain ($x = 0.05\text{m}$). (d) Difference between actual and predicted velocity profiles at mid-section of domain ($x = 0.05\text{m}$). These velocity profiles are derived from Flow Protocol 1A.

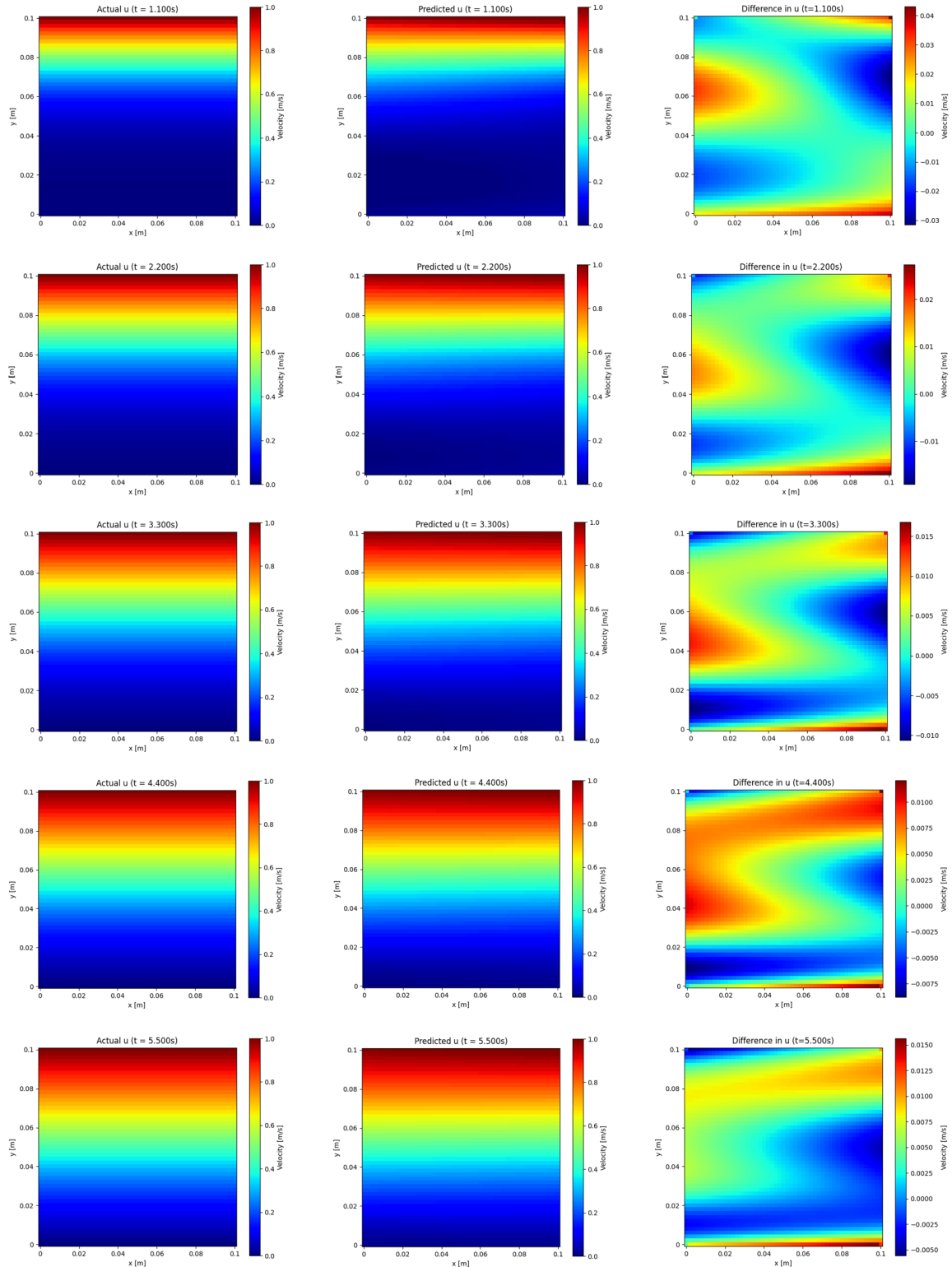


Fig. 12. Horizontal velocity profiles for the whole flow domain at $t = 1.1\text{s}, 2.2\text{s}, 3.3\text{s}, 4.4\text{s}$, and 5.5s . The left column represents the actual velocity profiles, the middle column represents the predicted velocity profiles, and the right column represents the discrepancy between both profiles. These velocity profiles are derived from Flow Protocol 1B.

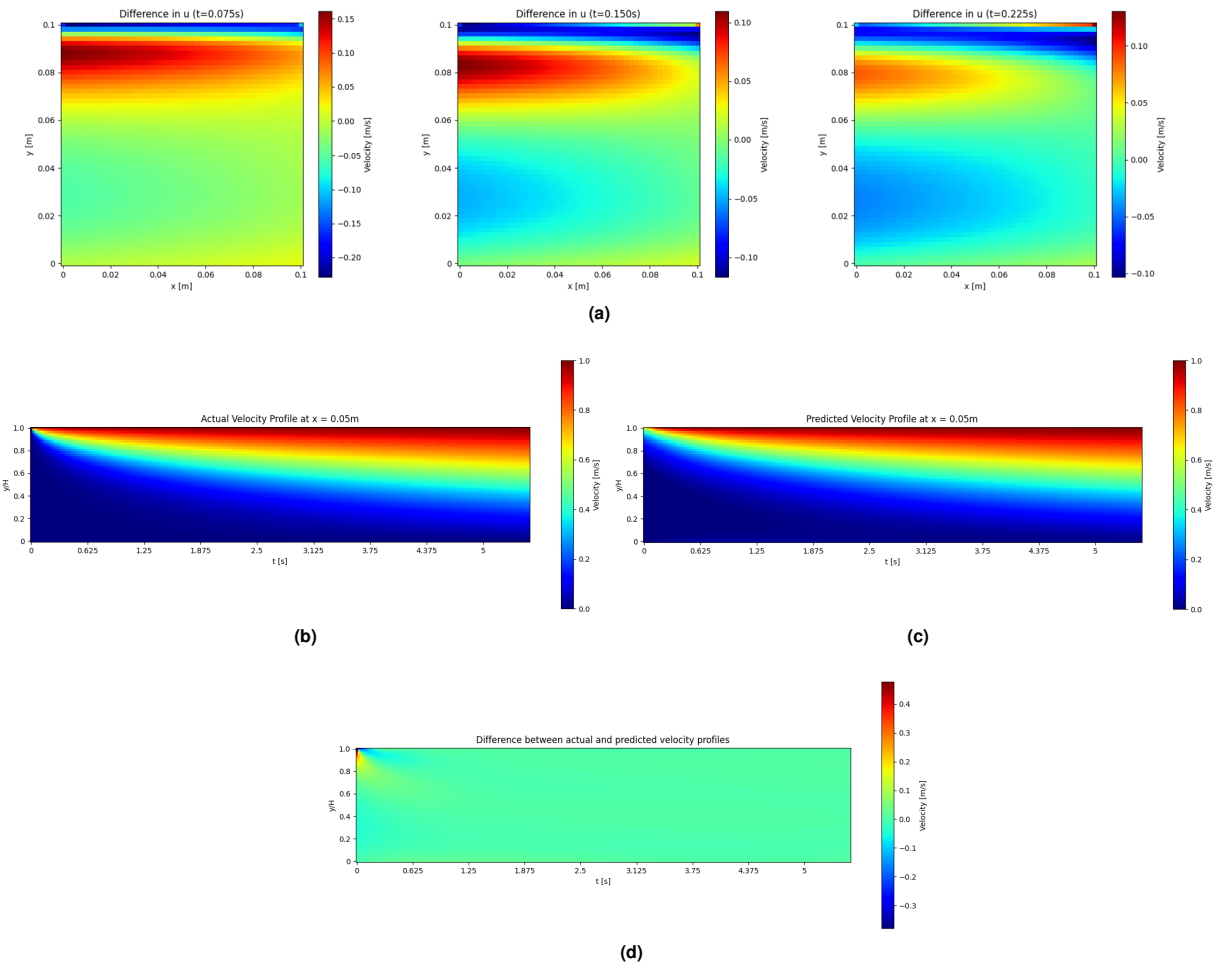


Fig. 13. (a) Discrepancy between actual and predicted horizontal velocity profiles for $t = 0.075\text{s}$, 0.15s , and 0.225s . (b) Actual velocity profile for entire flow duration at mid-section of domain ($x = 0.05\text{m}$). (c) Predicted velocity profile for entire flow duration at mid-section of domain ($x = 0.05\text{m}$). (d) Difference between actual and predicted velocity profiles at mid-section of domain ($x = 0.05\text{m}$). These velocity profiles are derived from Flow Protocol 1B.

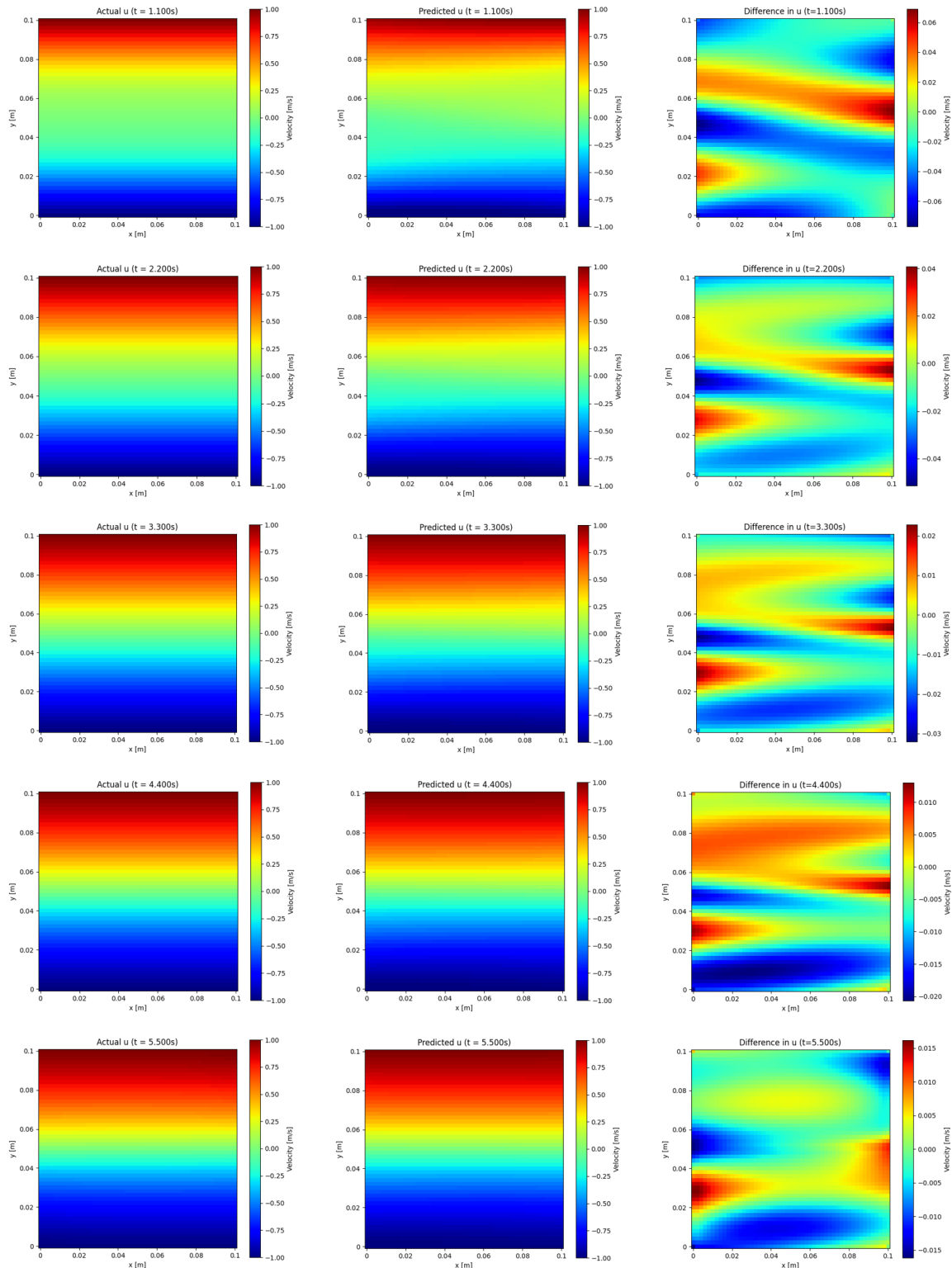


Fig. 14. Horizontal velocity profiles for the whole flow domain at $t = 1.1s, 2.2s, 3.3s, 4.4s$, and $5.5s$. The left column represents the actual velocity profiles, the middle column represents the predicted velocity profiles, and the right column represents the discrepancy between both profiles. These velocity profiles are derived from Flow Protocol 2A.

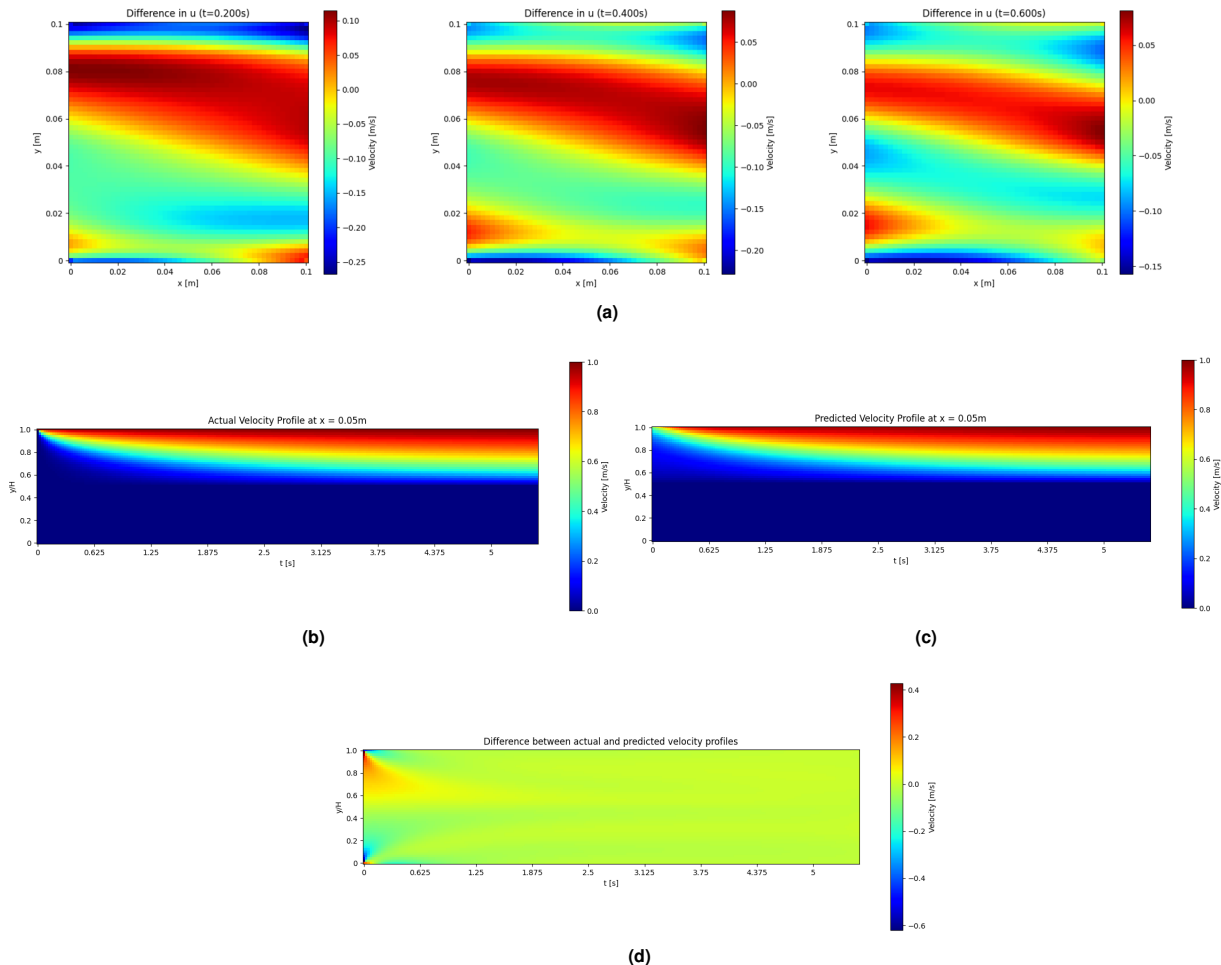


Fig. 15. (a) Discrepancy between actual and predicted horizontal velocity profiles for $t = 0.2\text{s}$, 0.4s , and 0.6s . (b) Actual velocity profile for entire flow duration at mid-section of domain ($x = 0.05\text{m}$). (c) Predicted velocity profile for entire flow duration at mid-section of domain ($x = 0.05\text{m}$). (d) Difference between actual and predicted velocity profiles at mid-section of domain ($x = 0.05\text{m}$). These velocity profiles are derived from Flow Protocol 2A.

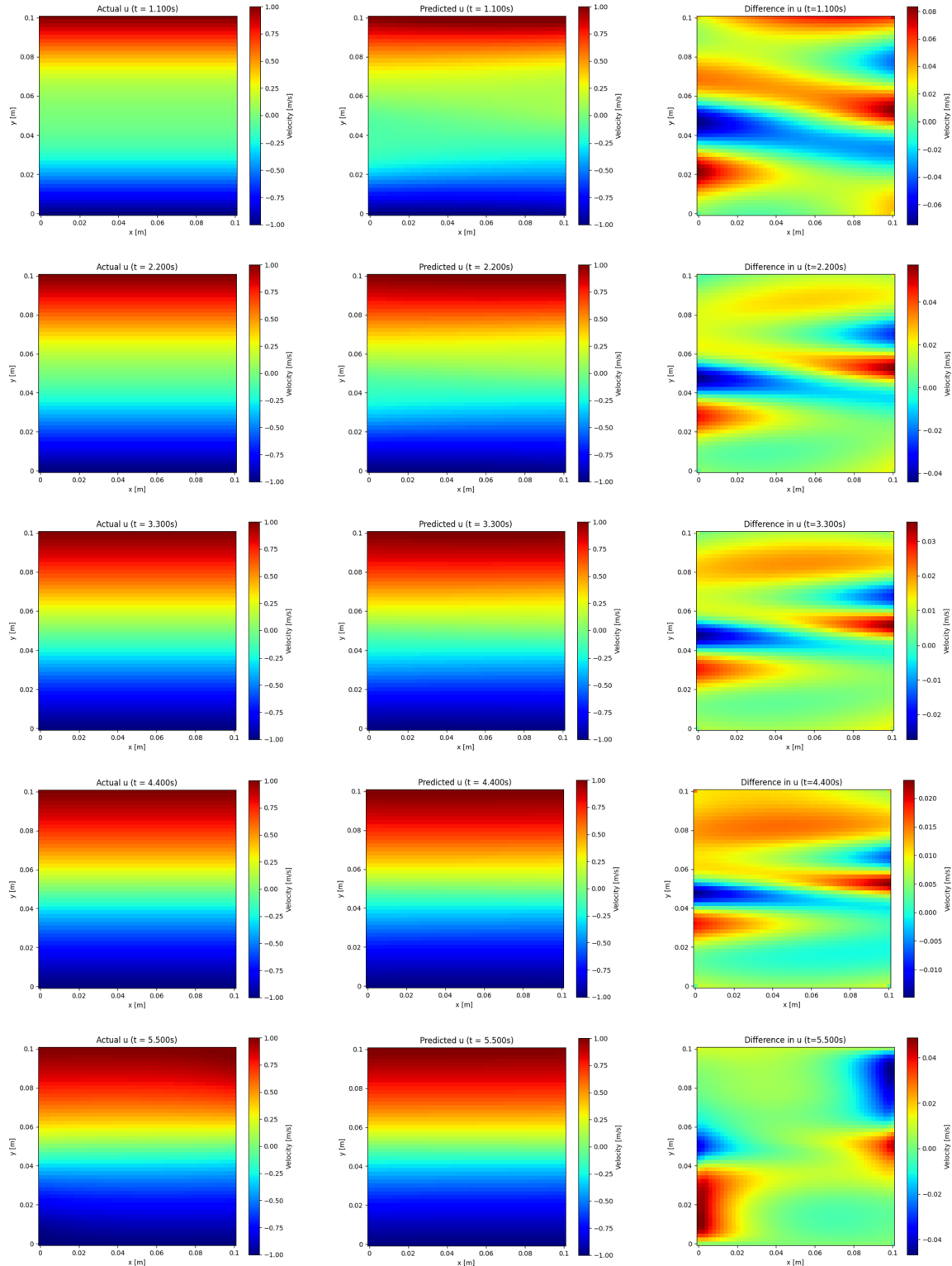


Fig. 16. Horizontal velocity profiles for the whole flow domain at $t = 1.1\text{s}, 2.2\text{s}, 3.3\text{s}, 4.4\text{s}$, and 5.5s . The left column represents the actual velocity profiles, the middle column represents the predicted velocity profiles, and the right column represents the discrepancy between both profiles. These velocity profiles are derived from Flow Protocol 2B.

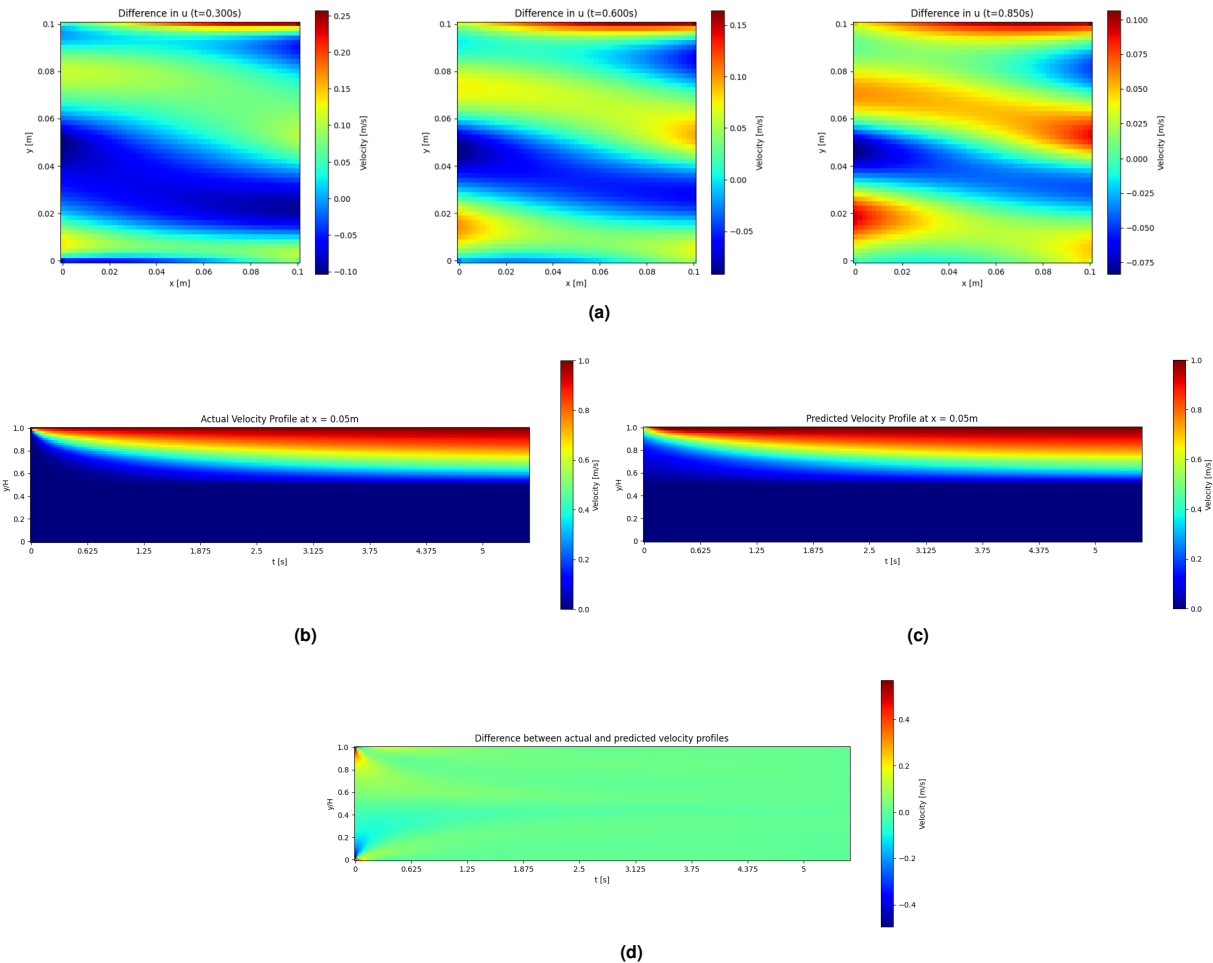


Fig. 17. (a) Discrepancy between actual and predicted horizontal velocity profiles for $t = 0.3\text{s}$, 0.6s , and 0.85s . (b) Actual velocity profile for entire flow duration at mid-section of domain ($x = 0.05\text{m}$). (c) Predicted velocity profile for entire flow duration at mid-section of domain ($x = 0.05\text{m}$). (d) Difference between actual and predicted velocity profiles at mid-section of domain ($x = 0.05\text{m}$). These velocity profiles are derived from Flow Protocol 2B.

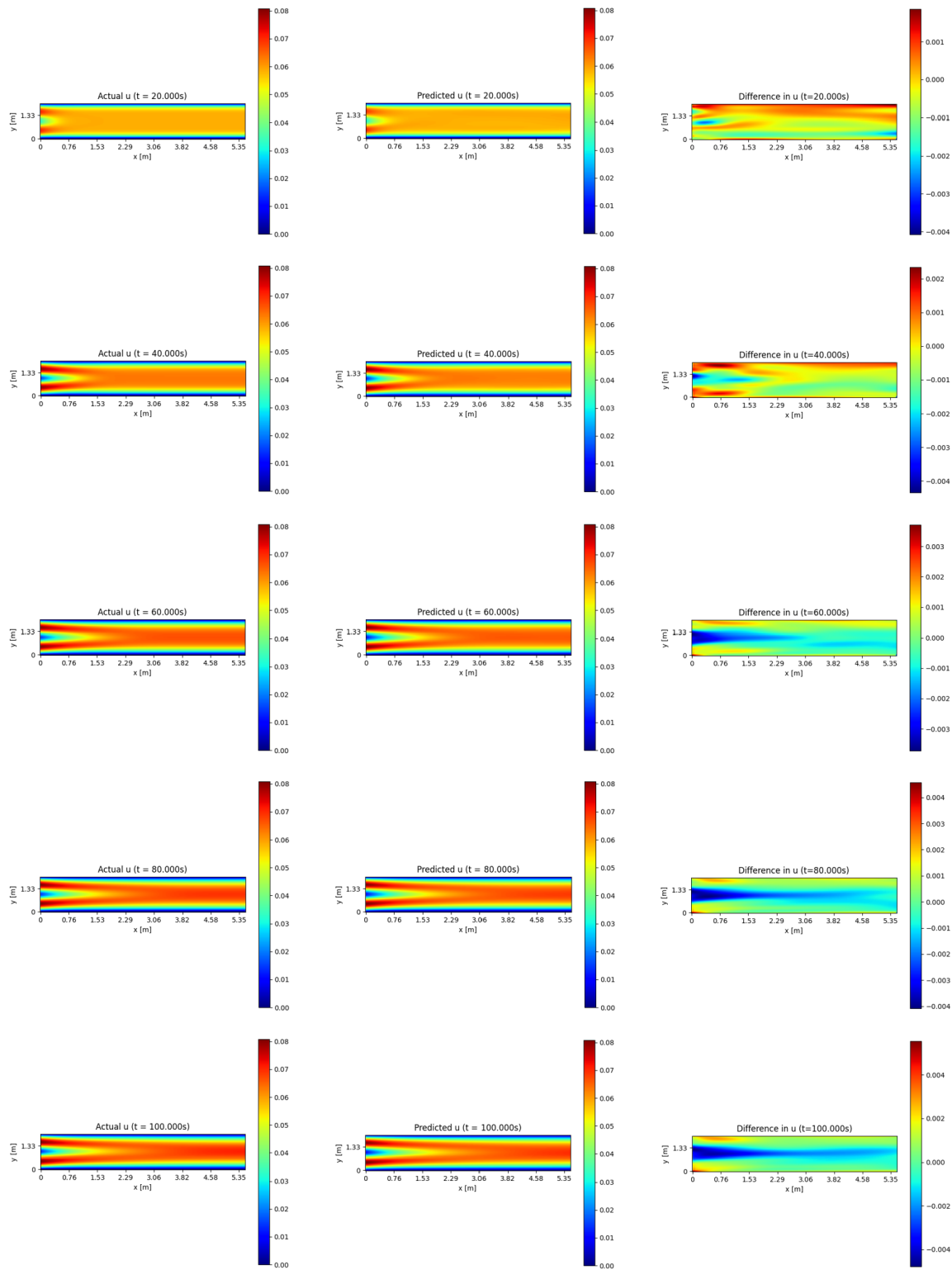


Fig. 18. Horizontal velocity profiles for the whole flow domain at $t = 20s, 40s, 60s, 80s$, and $100s$. The left column represents the actual velocity profiles, the middle column represents the predicted velocity profiles, and the right column represents the discrepancy between both profiles. These velocity profiles are derived from Flow Protocol 3A.

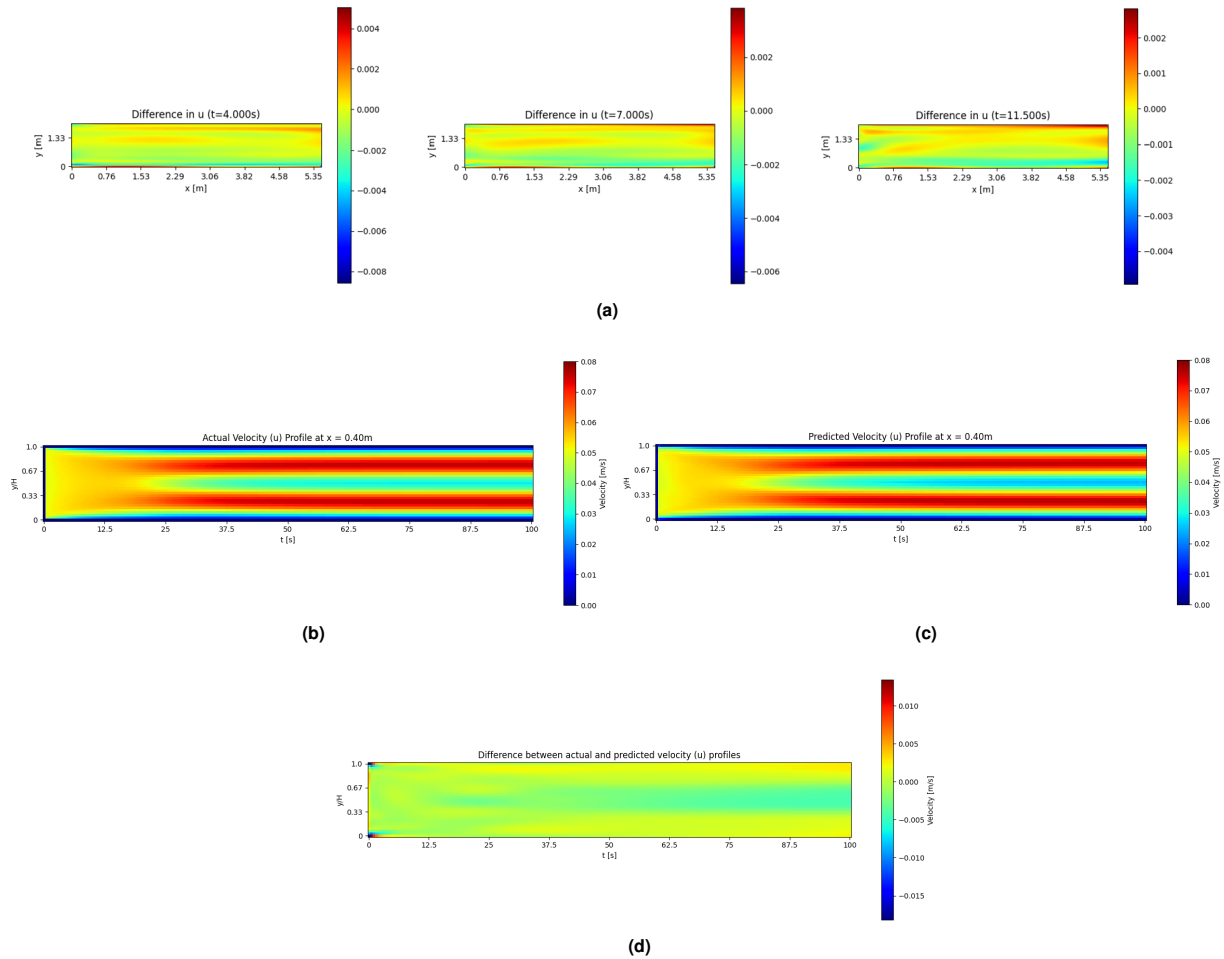


Fig. 19. (a) Discrepancy between actual and predicted horizontal velocity profiles for $t = 4s$, $7s$, and $11.5s$. (b) Actual velocity profile for entire flow duration at domain of interest ($x = 0.40m$). (c) Predicted velocity profile for entire flow duration at domain of interest ($x = 0.40m$). (d) Difference between actual and predicted velocity profiles at domain of interest ($x = 0.40m$). These velocity profiles are derived from Flow Protocol 3A.

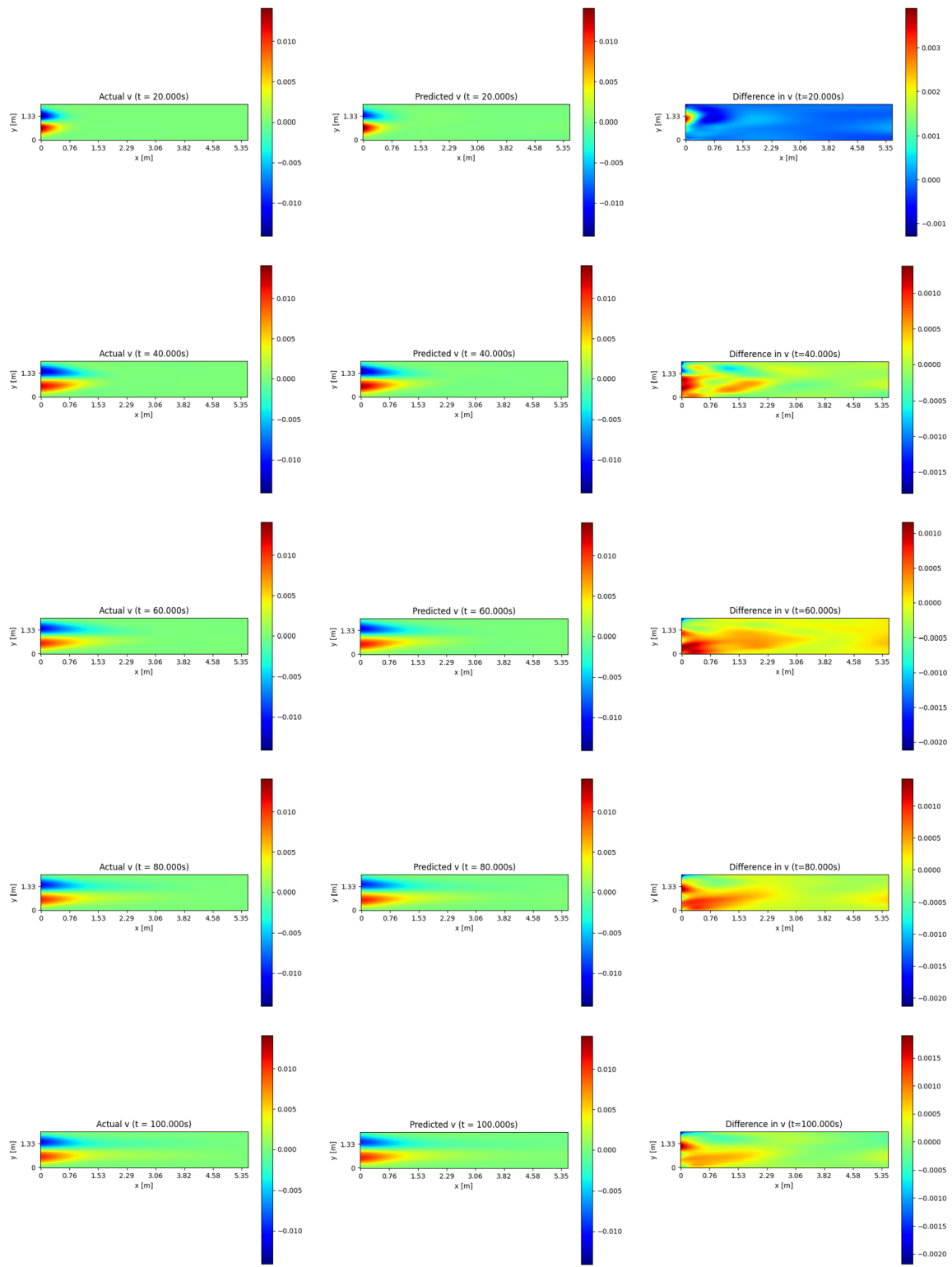


Fig. 20. Vertical velocity profiles for the whole flow domain at $t = 20\text{s}$, 40s , 60s , 80s , and 100s . The left column represents the actual velocity profiles, the middle column represents the predicted velocity profiles, and the right column represents the discrepancy between both profiles. These velocity profiles are derived from Flow Protocol 3A.

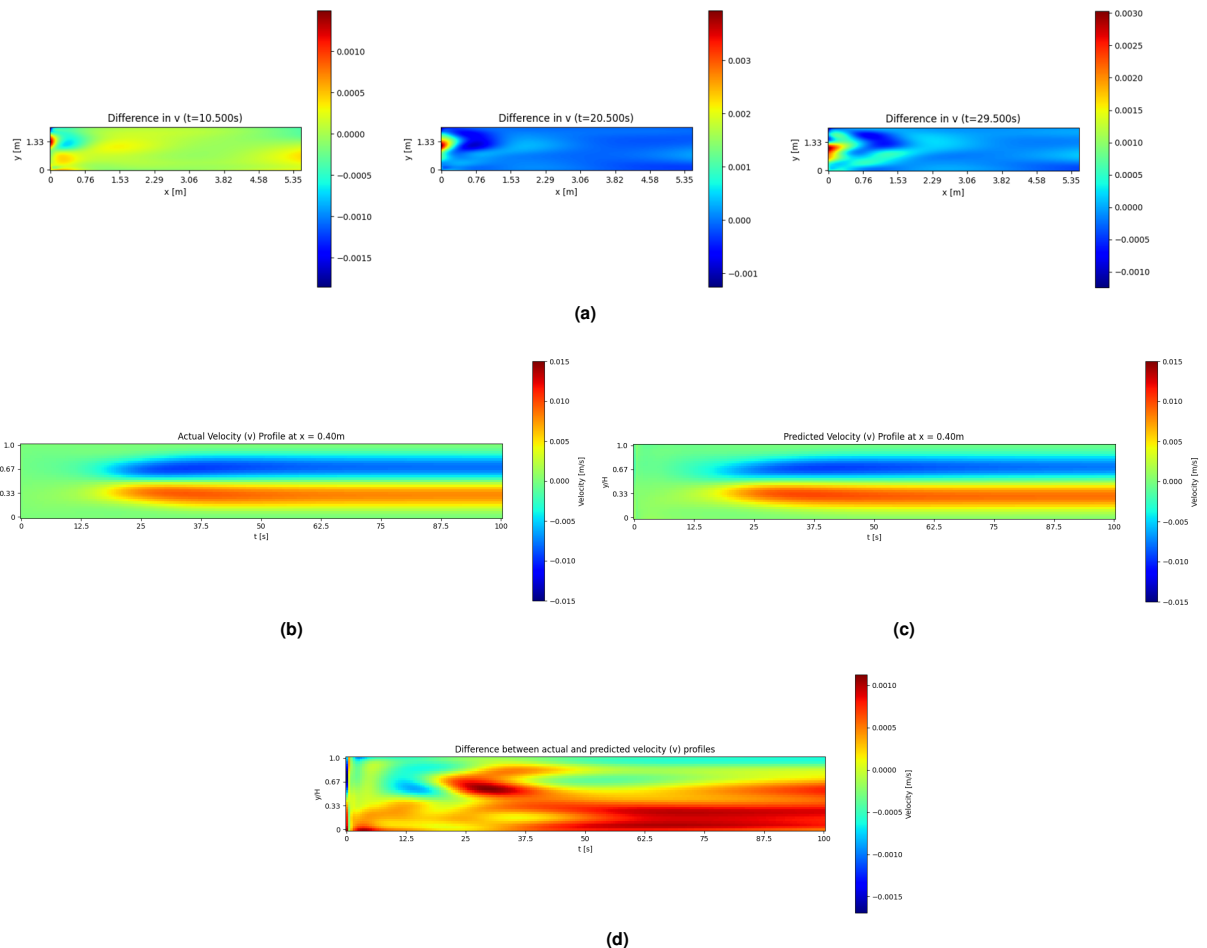


Fig. 21. (a) Discrepancy between actual and predicted vertical velocity profiles for $t = 10.5\text{s}$, 20.5s , and 29.5s . (b) Actual velocity profile for entire flow duration at domain of interest ($x = 0.40\text{m}$). (c) Predicted velocity profile for entire flow duration at mid-section of domain of interest ($x = 0.40\text{m}$). (d) Difference between actual and predicted velocity profiles at domain of interest ($x = 0.40\text{m}$). These velocity profiles are derived from Flow Protocol 3A.

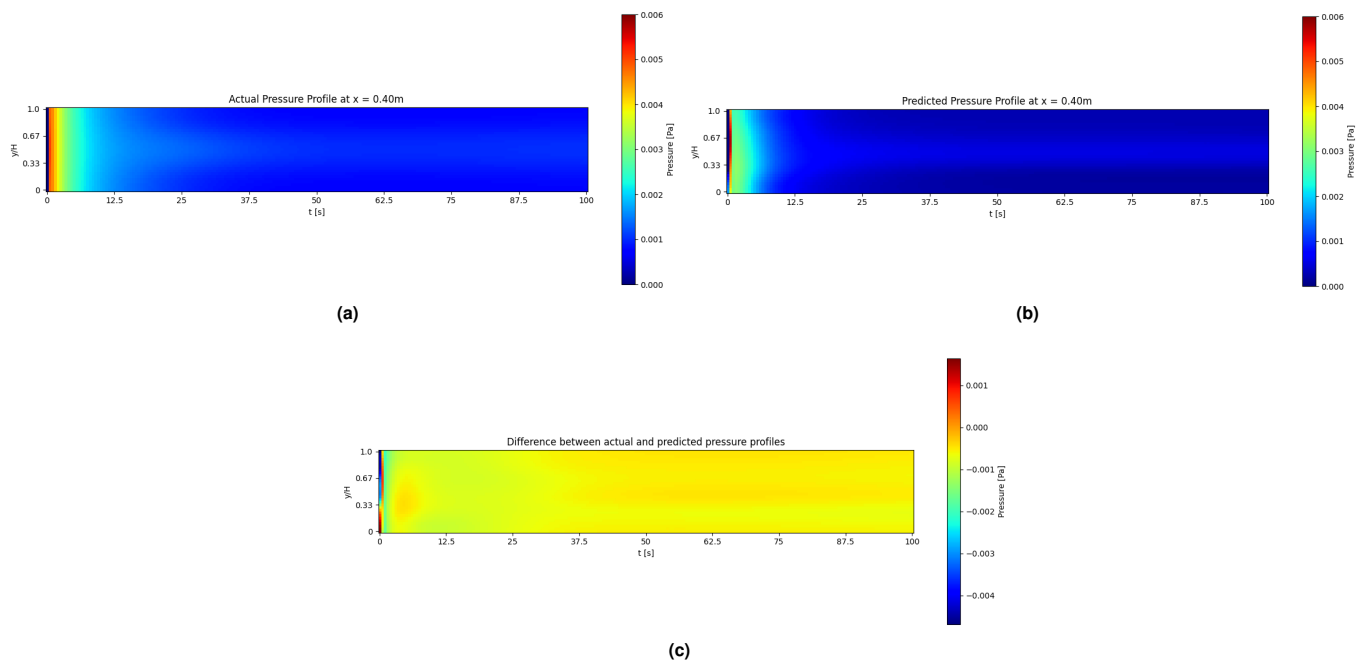


Fig. 22. (a) Actual pressure profile for entire flow duration at domain of interest ($x = 0.40\text{m}$). (b) Predicted pressure profile for entire flow duration at domain of interest ($x = 0.40\text{m}$). (c) Difference between actual and predicted pressure profiles at domain of interest ($x = 0.40\text{m}$). These pressure profiles are derived from Flow Protocol 3A.

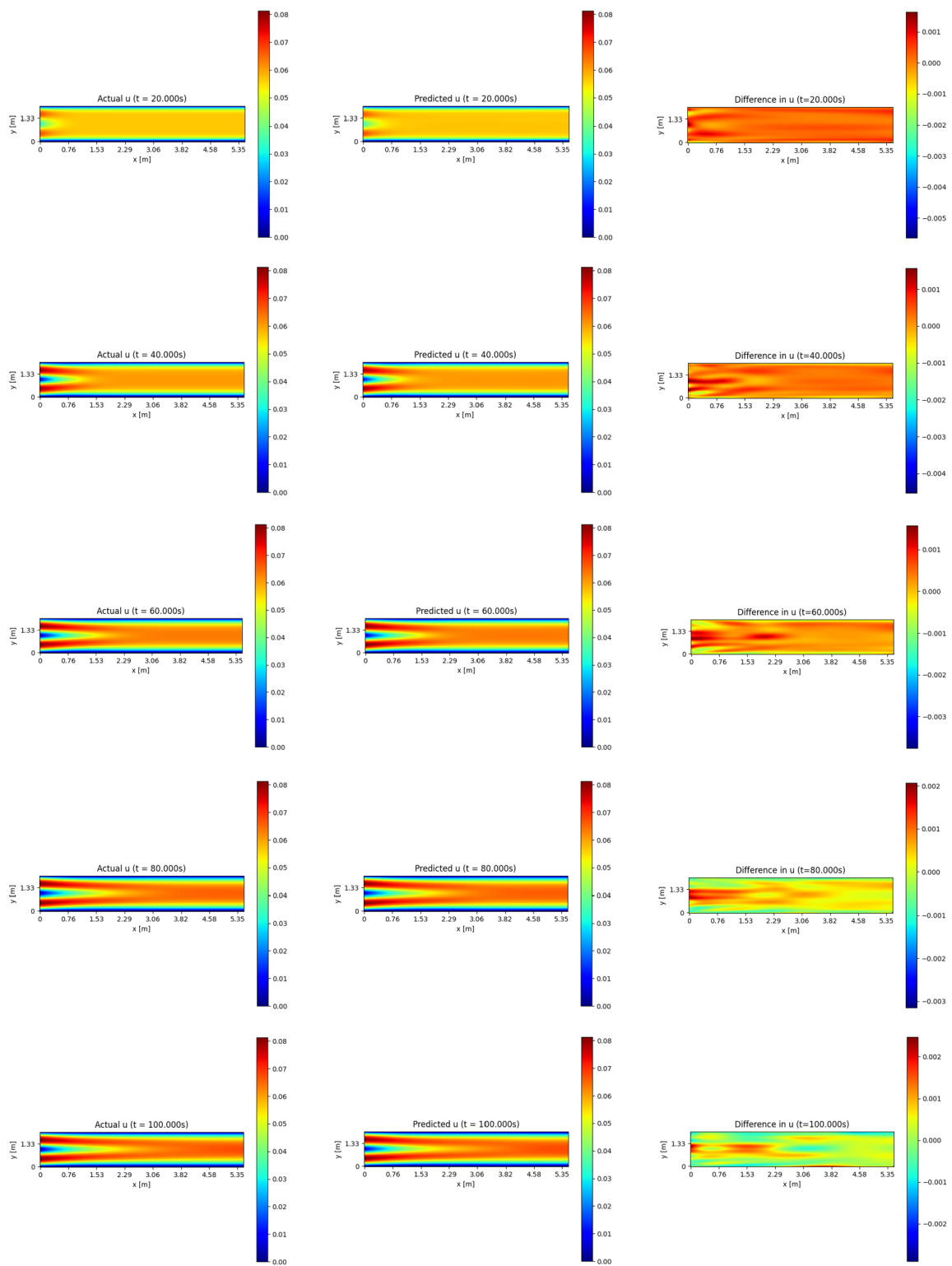


Fig. 23. Horizontal velocity profiles for the whole flow domain at $t = 20\text{s}$, 40s , 60s , 80s , and 100s . The left column represents the actual velocity profiles, the middle column represents the predicted velocity profiles, and the right column represents the discrepancy between both profiles. These velocity profiles are derived from Flow Protocol 3B.

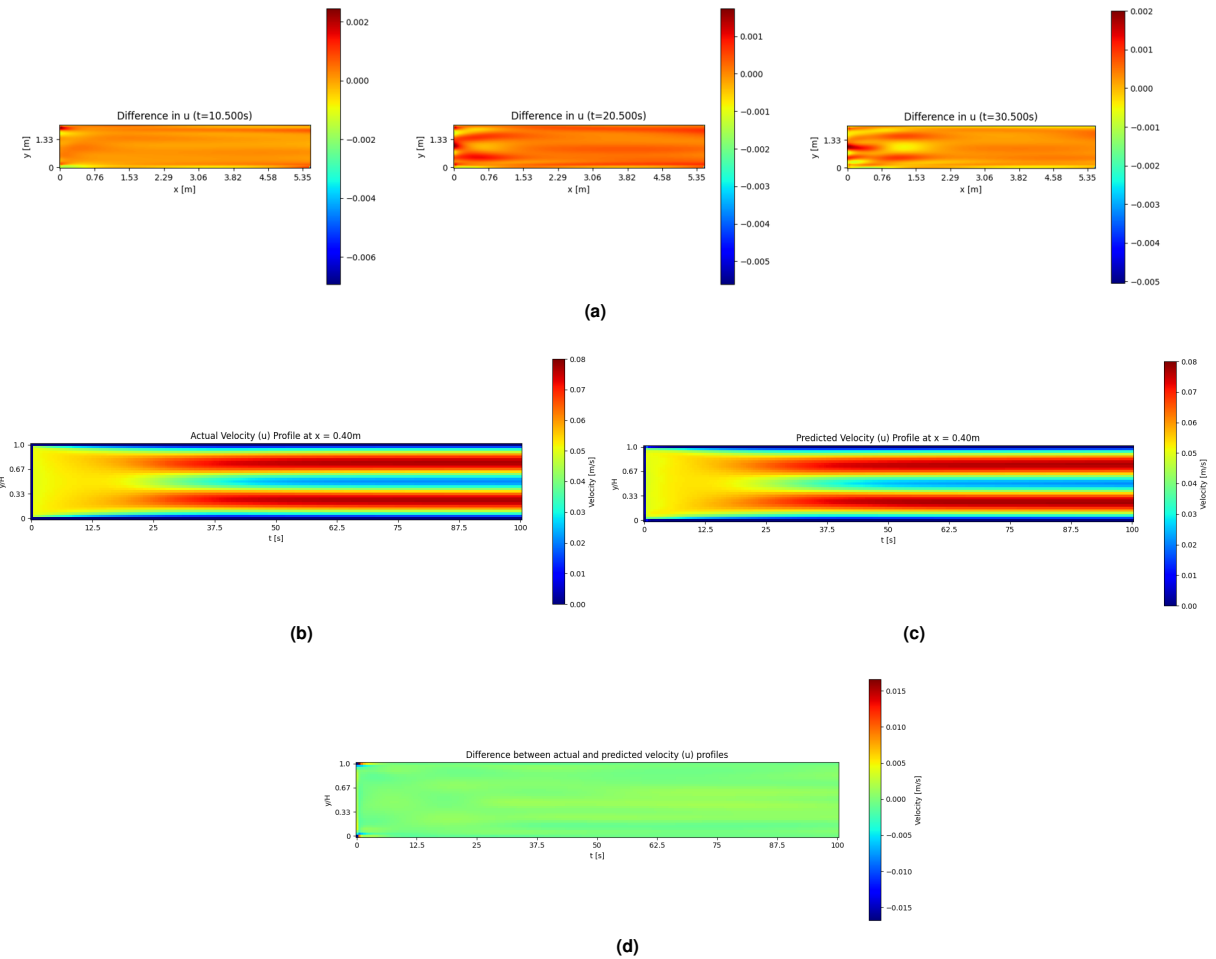


Fig. 24. (a) Discrepancy between actual and predicted vertical velocity profiles for $t = 10.5\text{s}$, 20.5s , and 30.5s . (b) Actual velocity profile for entire flow duration at domain of interest ($x = 0.40\text{m}$). (c) Predicted velocity profile for entire flow duration at mid-section of domain of interest ($x = 0.40\text{m}$). (d) Difference between actual and predicted velocity profiles at domain of interest ($x = 0.40\text{m}$). These velocity profiles are derived from Flow Protocol 3B.

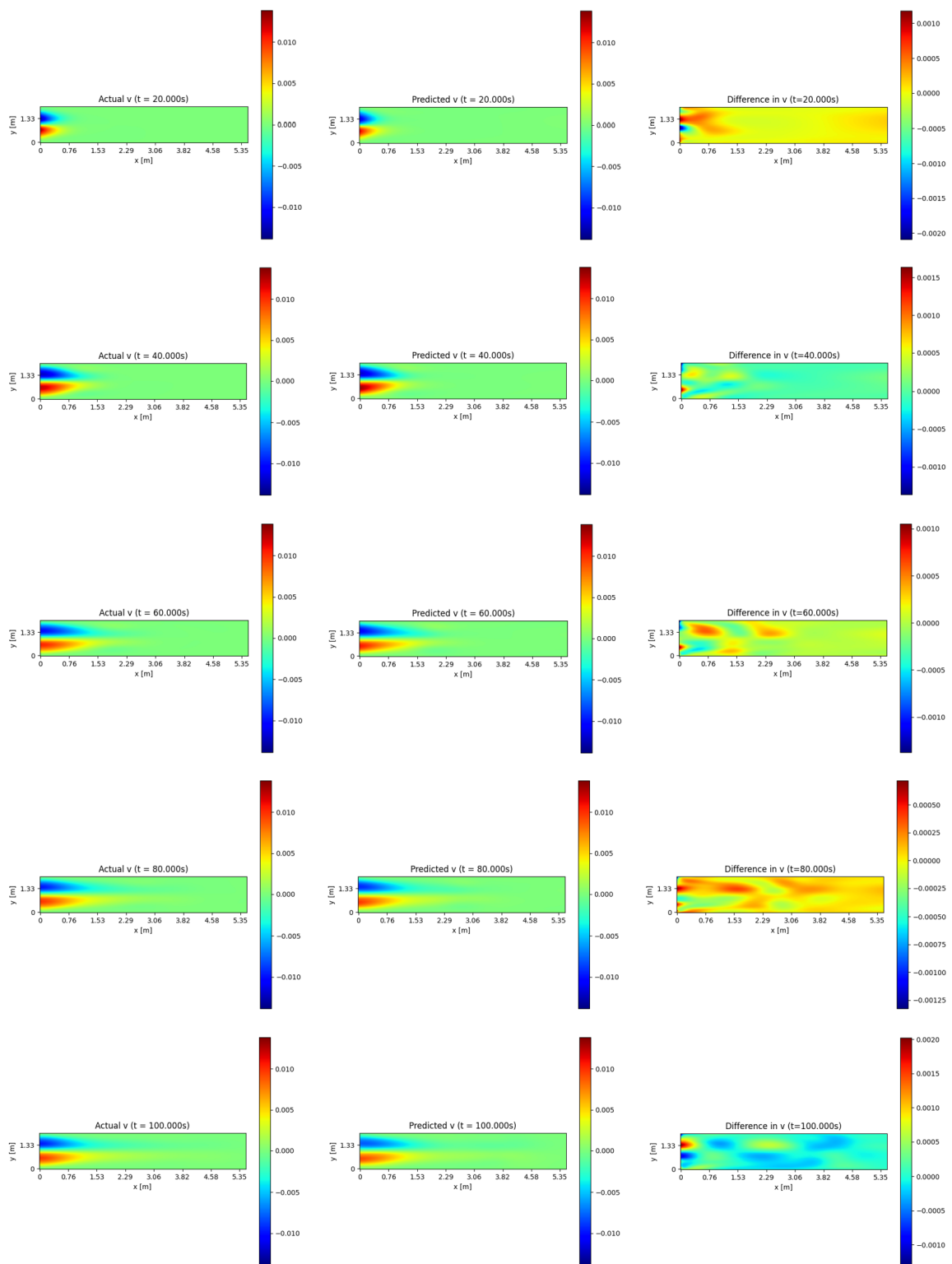


Fig. 25. Vertical velocity profiles for the whole flow domain at $t = 20s, 40s, 60s, 80s$, and $100s$. The left column represents the actual velocity profiles, the middle column represents the predicted velocity profiles, and the right column represents the discrepancy between both profiles. These velocity profiles are derived from Flow Protocol 3B.

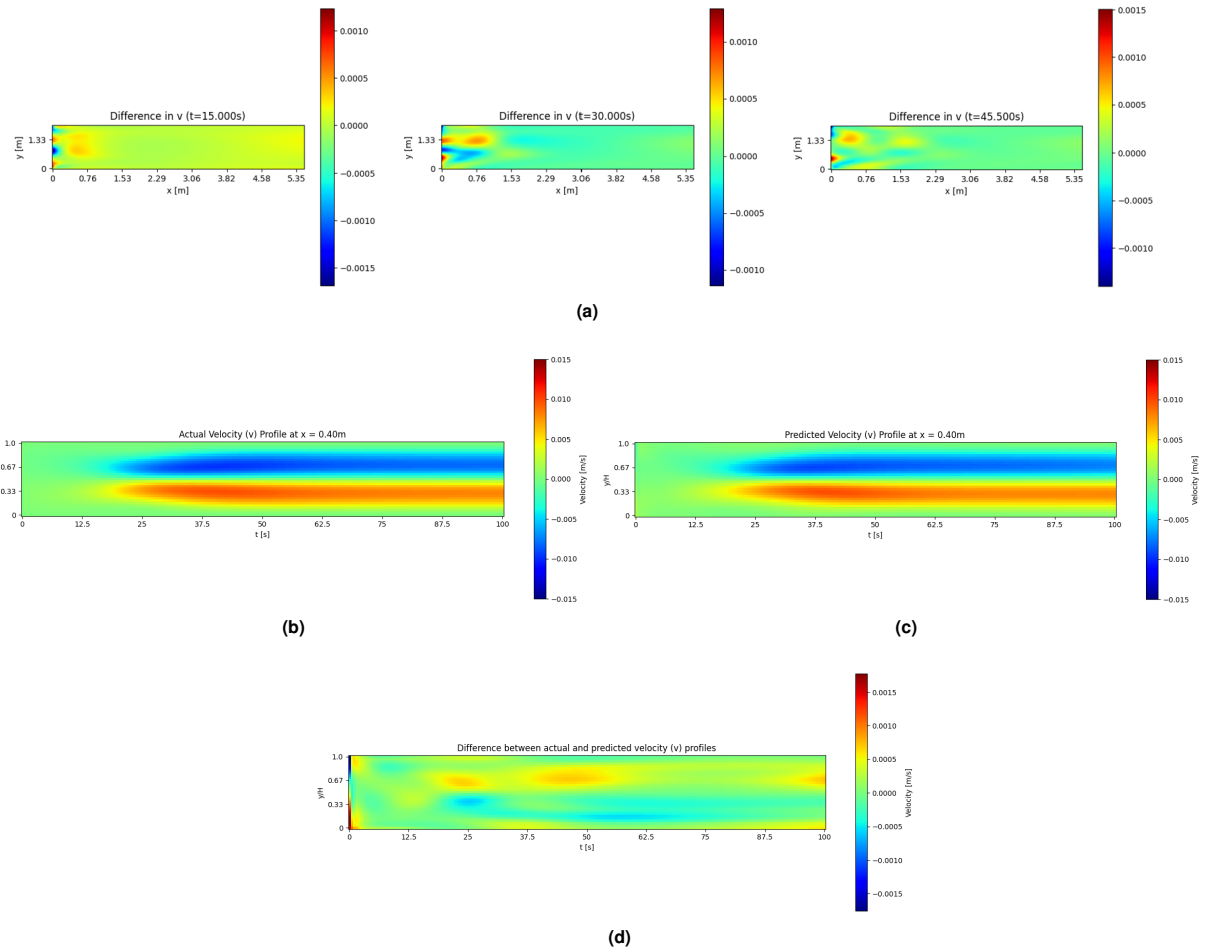


Fig. 26. (a) Discrepancy between actual and predicted vertical velocity profiles for $t = 15s$, $30s$, and $45.5s$. (b) Actual velocity profile for entire flow duration at domain of interest ($x = 0.40m$). (c) Predicted velocity profile for entire flow duration at mid-section of domain of interest ($x = 0.40m$). (d) Difference between actual and predicted velocity profiles at domain of interest ($x = 0.40m$). These velocity profiles are derived from Flow Protocol 3B.

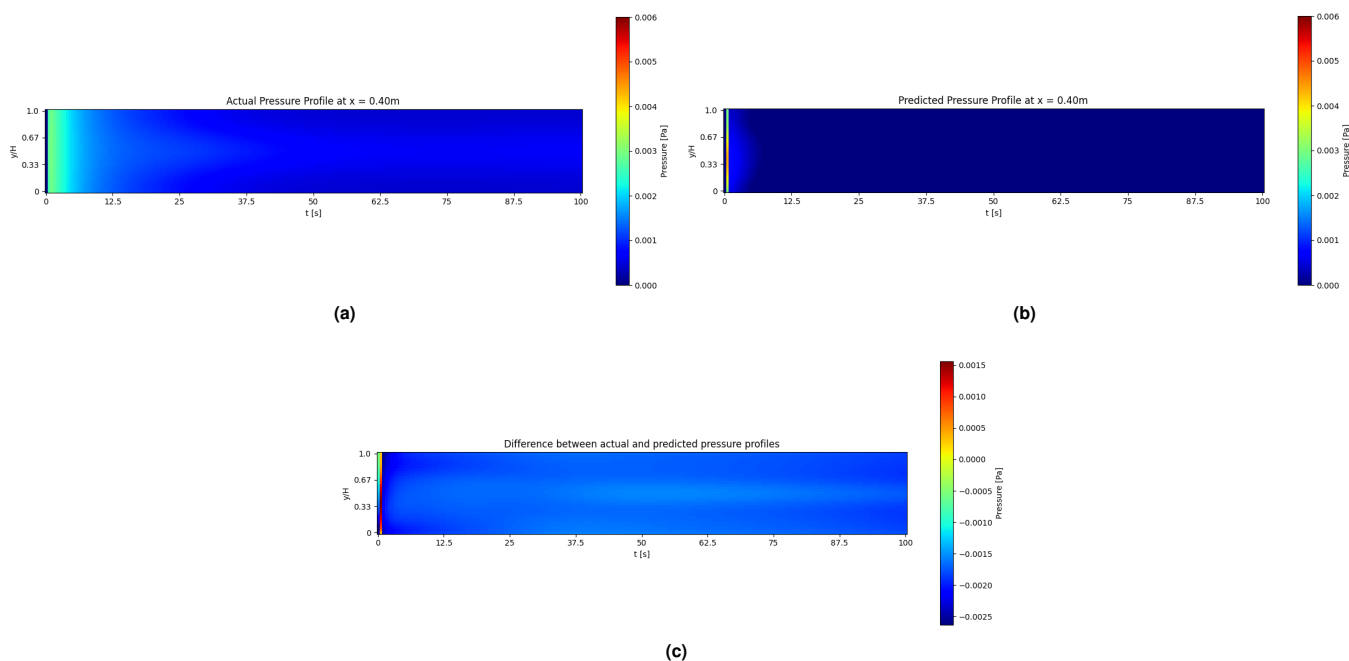


Fig. 27. (a) Actual pressure profile for entire flow duration at domain of interest ($x = 0.40m$). (b) Predicted pressure profile for entire flow duration at domain of interest ($x = 0.40m$). (c) Difference between actual and predicted pressure profiles at domain of interest ($x = 0.40m$). These pressure profiles are derived from Flow Protocol 3B.